

**Design and Optimization of x-y- θ_z
Cylindrical Flexure Stage**

by

Laura Yu Matloff

Submitted to the Department of Mechanical Engineering
in partial fulfillment of the requirements for the degree of

Bachelor of Science in Mechanical Engineering

at the

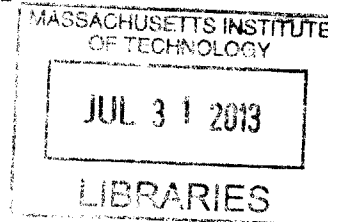
MASSACHUSETTS INSTITUTE OF TECHNOLOGY

June 2013

©2013 Laura Yu Matloff. All rights reserved.

The author hereby grants to MIT permission to reproduce and to
distribute publicly paper and electronic copies of this thesis document in
whole or in part in any medium now known or hereafter created.

ARCHIVED



Author
.....

Department of Mechanical Engineering

May 17, 2013

Certified by
.....

Martin L. Culpepper

Associate Professor of Mechanical Engineering

Thesis Supervisor

Accepted by
.....

Anette Hosoi

Professor of Mechanical Engineering

Undergraduate Officer

Design and Optimization of x - y - θ_z Cylindrical Flexure Stage

by

Laura Yu Matloff

Submitted to the Department of Mechanical Engineering
on May 17, 2013, in partial fulfillment of the
requirements for the degree of
Bachelor of Science in Mechanical Engineering

Abstract

Cylindrical flexures (CFs) are composed of curved beams whose length is defined by a radius, R , and a sweep angle, φ , [1]. The curved nature of the beams results in additional kinematics, requiring additional design rules beyond those used for straight-beam flexures. The curvature also adds additional parameters that allow for adjustments, suggesting that CFs may meet requirements that cannot be met with straight-beams. CFs have the potential to further open the flexure design space. In this study, cylindrical flexure design rules and models were used to optimize an x - y - θ_z stage design for a Dip-pen nanolithography (DPN) application. DPN a nanometer-scale fabrication technology that uses an atomic force microscope (AFM) cantilevered tip to place chemical compounds on a substrate. The flexure designed aids in alignment of the tip relative to the machine, increasing accuracy and repeatability.

The first step to design a flexure system is applying CF design rules to create a system that best fits functional requirements. Several different system configurations were considered, since reaching an optimal design is a highly iterative process. Once the best configuration was determined, element parameters were optimized using CF design rules. The optimized design was then corroborated using finite element analysis (FEA). The CF design rules greatly informed the design, reducing time spent on FEA by quickly narrowing in on successful designs. The finalized flexure design was fabricated using a waterjet machine and placed in a testing apparatus designed to measure predicted stiffnesses and verify functionality.

The CF model predicted the final measurements quite closely, although there were variability in the measurements and simplifications in the model. In K_{θ_x} , the error was as small as 0.3%, while the other stiffnesses had errors around 30%, except for K_x , which is twice as stiff than the model. This could be due to the simplification of more complicated tip boundary condition effects in the model or error in measurement of the fabricated flexure.

Although the model did not predict the final stiffness values exactly, it was critical in reducing time spent optimizing the system by quickly determining key parameters. The process of design and optimization shed light on advantages and disadvantages of using cylindrical flexures for an x - y - θ_z stage in general, and demonstrated the usability of CF rules. Observations from this research augmented the design guidelines, which will help others design CFs for other functional requirements.

Thesis Supervisor: Martin L. Culpepper

Title: Associate Professor of Mechanical Engineering

Acknowledgments

To Professor Martin Culpepper: Beyond being just a thesis advisor, you have been a great mentor, guiding me through MIT and giving me advice for graduate school and beyond. It has been a pleasure to be able to work with you, and thank you so much for all of your help and support; I have definitely grown under your tutelage.

To Maria Telleria: Thank you for sharing your thesis work with me and choosing me for a senior thesis mentee. I am so privileged to have been able to work with you and learn from you. I look forward to the day your CF flexure design rules will be widely used!

To the other students in the PCSL lab, Bob, Marcel and Jon: Thank you for helping me by sharing your expertise and your experiences. I truly appreciate all your questions and encouragements that have helped me further develop my thesis.

To Bill Buckley, LMP Lab Manager: Your shop expertise is tremendous, and it has been my honor to learn from you. Thank you also for your guidance in manufacturing the flexure; it would not exist if not for your help!

To my first academic advisor, Professor Kimberly Hamad-Schifferli: You have been there for me from the start, helping me when I was struggling, and later, really helping me thrive. Thank you for going above and beyond as an advisor!

To my second academic advisor, Professor Derek Rowell: You were a perfect senior year advisor, helping me choose my final classes at MIT and imparting with me your wisdom and humor.

To everyone at MIT: Thank you for making my MIT experience unforgettable. I have developed a healthy respect for my brilliant peers, and without them, I would not have learned as much, nor have had so much fun. And to my professors, who have given me the greatest gift of knowledge, thank you.

Contents

1	Introduction	15
1.1	Cylindrical Flexures	16
1.1.1	Flexure Background	16
1.1.2	Benefits and Challenges of Cylindrical Flexures	18
1.1.3	Design Rules of CFs	20
1.2	Prior Art in x - y - θ_z Stages	23
1.3	Dip Pen Nanolithography	27
2	Design	29
2.1	Design Goals and Functional Requirements	29
2.2	Design Process	31
2.2.1	Loading Behaviour of a Single r -compliance Flexure Element	31
2.2.2	Two, Three, and Four Element Systems	32
2.2.3	Four-element Off-axis System (Spider Flexure)	35
2.2.4	Serial Four-element System (Serial Spider Flexure)	40
2.3	Final Design - Concept Optimization and Verification	43
2.3.1	System Model [5]	43
2.3.2	Modal Analysis	45
2.3.3	Finite Element Analysis Corroborations	47
2.3.4	Fabrication	50

3	Measurement and Testing	53
3.1	Measurement and Apparatus Design	53
3.2	Test Set-up and Measurement Techniques	54
4	Results and Analysis	57
4.1	Measured Values Compared to FEA and Model Values	57
4.2	Parasitic Motions	59
5	Conclusions and Future Work	61
	Bibliography	63

List of Figures

1-1	The final flexure design machined from 6061-T6 Aluminum	16
1-2	FACT design guidelines for straight-beam flexures in parallel and serial configurations [3]	17
1-3	General parameters of a CF element include radius of curvature, R , sweep angle, φ , radial thickness, t_r , and axial thickness, t_a . The flexure length is found by multiplying R by φ	18
1-4	General parameters of a CF element include radius of curvature, R , sweep angle, φ , radial thickness, t_r , and axial thickness, t_a . The flexure length is found by multiplying R by φ	19
1-5	Stiffness ratios for an r -compliance flexure element K_r/K_z and K_r/K_θ plotted against sweep angle, φ	20
1-6	Design steps to determine CF system compliance matrix using CF design rules. [5]	23
1-7	Basic straight-beam x-y- θ_z stage configuration [2]	24
1-8	A simple four-bar flexure exhibits an undesired parasitic motion. A compound four-bar flexure of two simple four-bar flexures in series exploits symmetry to control unwanted parasitic motion [6].	25
1-9	A Solidworks model of a straight-beam x-y- θ_z stage using compound four-bar wire flexures and the calculated stiffnesses of the system. [5] [7]	26

1-10	a) Folded hinge flexure concept for a x - y - θ_z stage [9] b) Diagram of circular single-axis flexure hinge based design for a x - y - θ_z stage driven by piezoelectric actuators [8]	27
1-11	Dip pen nanolithography (DPN) schematic representation. An AFM tip is used to convey a liquid chemical compound onto a solid substrate. [13]	28
2-1	Resulting deflections and rotations in a single r -compliance element tip due to different loading conditions. The blue arrows denote the desired displacement while the green and maroon arrows show the parasitic displacement and rotation.	31
2-2	Resulting desired (blue) and parasitic (green) motions of a two-flexure system design. When actuated in any planar direction, motion in only two out of the four desired quadrants can be attained, making the two-flexure design unfit for an x - y - θ_z stage	32
2-3	Resulting desired (blue) and parasitic (green) motions of a three-flexure system design under F_y and M loads. For the bottom two flexures, the resulting motions are off-axis either to stage coordinate system or to the flexure element coordinate system, adding complexity to the system.	33
2-4	Resulting desired (blue) and parasitic (green) motions of a four-flexure system design under F_y and M loads. Symmetry cancels out the parasitic motion and decouples the X and Y motions, but also increases stiffnesses for θ_z	33
2-5	A comparison of the advantages and disadvantages of two, three, and four element systems designs. None of the three designs has a decisive advantage over the others [5].	34
2-6	Four-element, off-axis System configuration made up of elements with sweep angles of 180 degrees. Parasitic motions are cancelled out	35

2-7	Four-element off-axis system in-plane, normalized stiffnesses vs. element sweep angle, φ . Desired stiffnesses occur at sweep angles of greater than 180 degrees. (K_x desired = 1700N/m, K_{θ_z} desired = 2Nm/rad, $R_{sys} = 3$ in, $R_{stage} = 0.5$ in, $t_z = 0.5$ in, $t_r = 0.024$ in, 6061-T6 Al)	37
2-8	Four-element Off-axis System with added attachment angle, η	38
2-9	Four-element off-axis system stiffness ratios vs. element sweep angle, φ . The stiffness ratios at 180 degrees and greater are undesirably high. ($R_{sys} = 3$ in, $R_{stage} = 0.5$ in, $t_z = 0.5$ in, $t_r = 0.024$ in, 6061-T6 Al)	39
2-10	FEA of a single CF element with large sweep angle shows twist in ΔZ which makes system less stiff compared to a straight-beam flexure with similar z thickness.	40
2-11	Double decker system design with two 60-degree elements in series to replace the single 180 degree flexure arm used previously.	41
2-12	Four two-series element systems with stage attachment angle, η , and series attachment angle, ν , to help with stiffness ratios and monolithic machinability.	42
2-13	Normalized Serial Four-element system stiffnesses vs. flexure attachment angle, ν . ν lowers system stiffnesses in x and in θ_z , but is limited to be less than or equal to 60 degrees in order to not alter R_{sys} . ($\varphi=60$ deg, $R_{sys} = 3$ in, $R_{stage} = 0.5$ in, $t_z = 0.5$ in, $t_r = 0.024$ in, 6061-T6 Al)	44
2-14	The first four frequency modes for CF Stage with the original design, four arms added, and arms with weights added.	46
2-15	FEA mesh of final flexure design. FEA was used to corroborate CF model results.	47
2-16	OMAX Waterjet machine path figure. The stage and flexures are constrained, and the flexure paths were cut first to minimize cutting error from vibration. The numbers denote the starting points and cutting order for the loops required for each flexure.	50

3-1 CAD model of measurement set up to verify flexure stiffnesses and functionality. Pulleys and weights are used to actuate the stage in a known direction with a given force 54

3-2 Photo of measurement test set up on optical table 56

4-1 FEA analysis on updated model that reflects real machined thicknesses and taper angle. Cross section of one element shows the average top and bottom thicknesses and taper angle. 58

List of Tables

2.1	Target DOF stiffnesses and ranges for flexure system driven by the actuator limitations.	30
2.2	Final specifications for CF x-y- θ_z stage element and system parameters . . .	45
2.3	Stiffness values determined by model and FEA calculations	48
2.4	FEA predictions for range in the three desired directions.	49
2.5	FEA calculations of the final CF flexure versus previous straight beam design straight beam [5] [7].	49
3.1	Summary of actuation forces used for measuring stiffness.	55
4.1	A comparison of system stiffness values as determined by CF model, FEA model, measured fabricated model, and updated FEA model with taper angles.	59
4.2	Voltage readings from capacitance probes measuring displacements in the parasitic directions compared to the variation (max – min) of the actuated directions. Due to availability of capacitance probes, only five directions could be measured at once.	60

Chapter 1

Introduction

This paper details the design process of an x - y - θ_z cylindrical flexure stage, that follows CF design rules and methodology. First, CF element behavior is studied to inform the choice of system configuration possibilities. Then, different configurations of CF systems are explored and modeled to determine the best configuration for an x - y - θ_z stage. These designs considered are then optimized to meet functional requirements following an iterative process to determine the best design.

In this case, an x - y - θ_z cylindrical flexure stage has been created to meet the needs for a dip pen nanolithography application (DPN). DPN technology places chemical compounds on a substrate at the nano-scale resolution using an atomic force microscope (AFM) cantilevered tip. The CF flexure would help position the AFM tips to the machine with greater accuracy and repeatability. The machined final flexure design can be seen in figure 1-1.

Applying CF rules in the design of the x - y - θ_z stage helps further the CF design rules by highlighting the advantages and disadvantages of using CFs, and unearthing potential new applications. This case study exemplifies usage of CF design rules, setting the stage for others to follow suit. CFs have the potential to fill a gap left by straight-flexures and expand the flexure design space, helping designers reach functional requirements they could not have before.

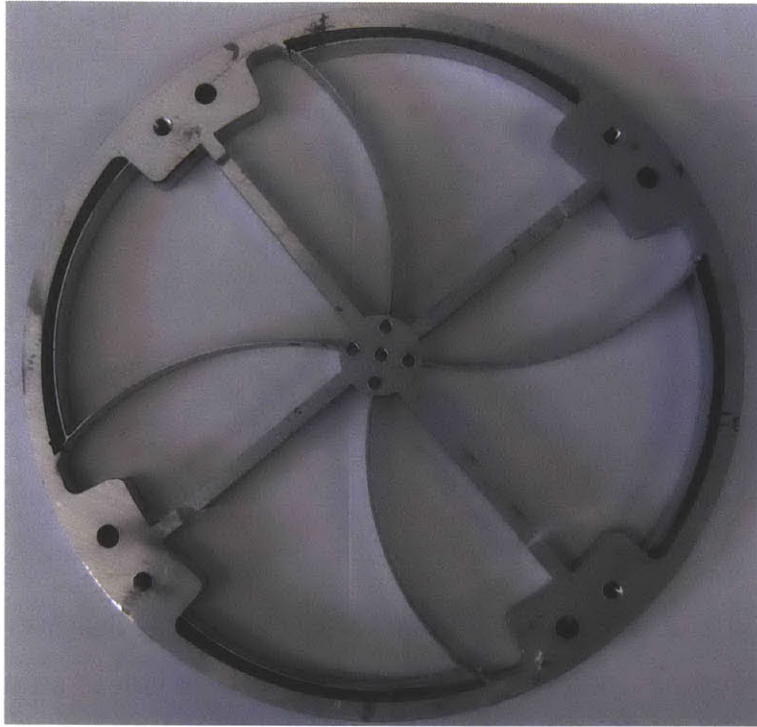


Figure 1-1: The final flexure design machined from 6061-T6 Aluminum

1.1 Cylindrical Flexures

1.1.1 Flexure Background

Flexures are mechanical structures that utilize material elasticity to allow certain motions, known as the element's degrees of freedom (DOFs), while constraining motion along the other directions. Elastic deformation of flexures results in a smooth motion usually in a small range. The elastic region of the material limits the operating range of a flexure, ensuring that the flexures do not permanently deform. Since flexure motion is due to material deformations on the molecular level, they avoid the unwanted effects of friction, stiction, and backlash [2]. Because of this property, they can be accurately controlled over small displacements and are commonly used for precision machines. Compliant flexures are useful machine elements, advantageous for high precision and low space requirements. Flexures are commonly fabricated from a single piece of material, and can

lower cost and assembly time.

Currently, rules and guidelines exist to help designers generate straight-beam flexure systems made up of any combination of flexures in parallel and series. One process to create flexure systems is the freedom and constraint topologies (FACT) method, a method that mathematically models the DOFs and constraints [3]. FACT is a systematic design process that helps designers determine system parameters, and the general guidelines used can be seen in figure 1-2.

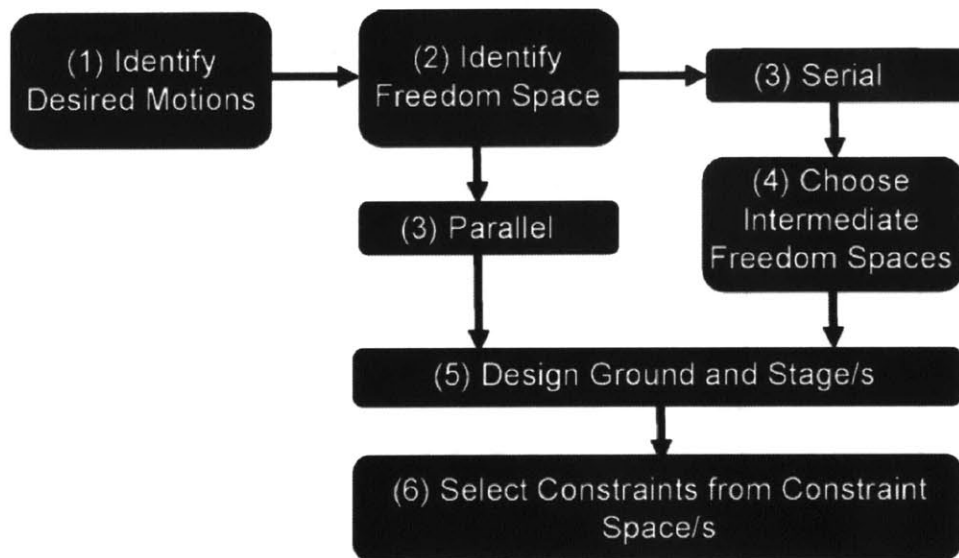


Figure 1-2: FACT design guidelines for straight-beam flexures in parallel and serial configurations [3]

While the usage of linear flexures has been much explored, the usage of cylindrical, or curved-beam, flexures is much less developed, although there exist many advantages to using them. They are more mathematically complicated to model and not as intuitive to use. Rules and guidelines applying the FACT methodologies have recently been developed for cylindrical flexures to help designers more easily meet their desired functional requirements using CFs, hopefully making CFs more widely used [4]. This project seeks to demonstrate the functionality of those design rules by applying them to a case study design for an x - y - θ_z stage.

1.1.2 Benefits and Challenges of Cylindrical Flexures

Cylindrical flexures are a specific type of flexure in which the flexure element's length is given by a radius of curvature, R , and a sweep angle, ϕ . The curvature of the beam element changes its mechanics making the current design rules for straight beam flexures inadequate for CF design. However, CFs have the advantage of having additional tuning parameters which give more flexibility in achieving functional requirements. Primarily in CFs, different sweep angles result in a variation in stiffness. The main parameters of a CF element, as illustrated in figure 1-3, are radius, R , sweep angle, ϕ , radial thickness, t_r , and axial thickness, t_a . R multiplied by ϕ gives the length of the flexure.

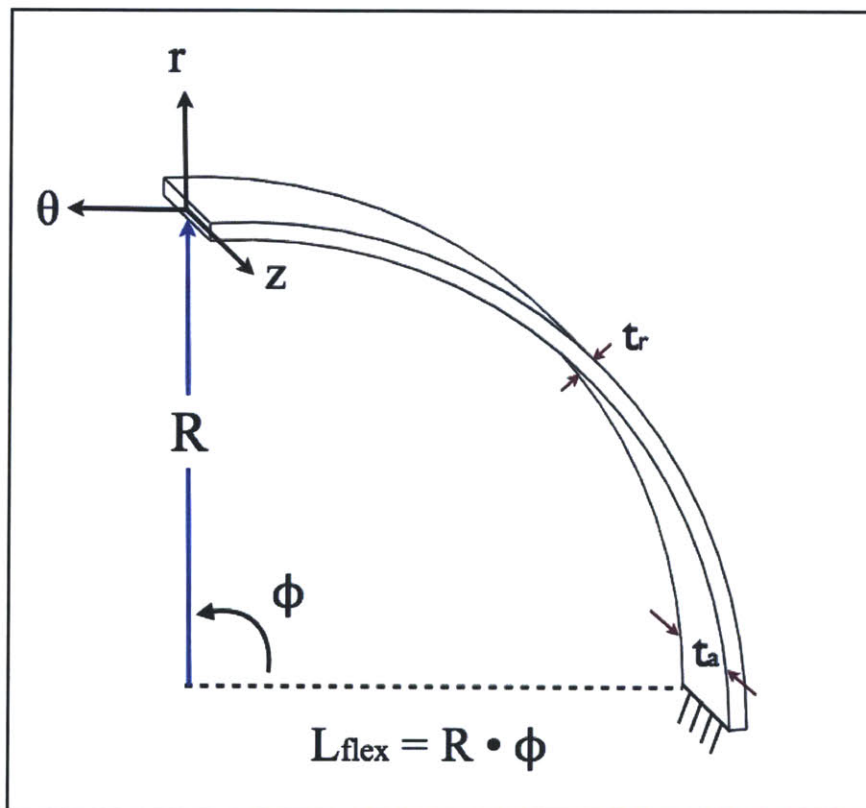


Figure 1-3: General parameters of a CF element include radius of curvature, R , sweep angle, ϕ , radial thickness, t_r , and axial thickness, t_a . The flexure length is found by multiplying R by ϕ .

Cylindrical flexures can be classified into two different types, z and r -compliance flexures depending on the relative thicknesses of t_r and t_a . In z -compliance flexures, t_a is the critical dimension, and is generally at least 6 times smaller than t_r . As a result, z -compliance flexures are more compliant in the z direction, but are stiffer in r and θ . For r -compliance flexures, it is reversed; t_r is the critical dimension, and is much smaller than t_a . r -compliance flexures are more compliant in r and θ , but are more stiff in z . This study focuses on r -compliance flexures, since they are more applicable for usage in an x - y - θ_z design. Figure 1-4 shows the configurations of both z and r -compliance flexures.

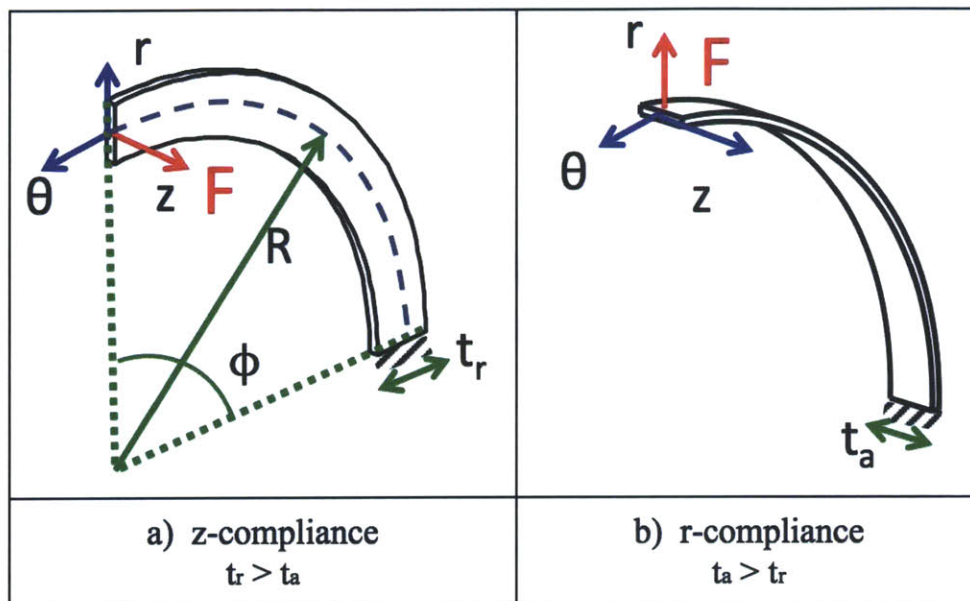


Figure 1-4: General parameters of a CF element include radius of curvature, R , sweep angle, ϕ , radial thickness, t_r , and axial thickness, t_a . The flexure length is found by multiplying R by ϕ .

The inspiration to use CFs for an x - y - θ_z stage stems from the fact that axial stiffness decreases rapidly with sweep angle in r -compliance flexures. This means a single beam can have 2 DOFs due to compliance in both r and θ directions, which may be helpful for an x - y - θ_z system configuration. This compliance in both r and θ directions also give rise to parasitic motions. Parasitic motions, or motions in undesired directions other than the one being actuated, are generally present in single flexure elements. They are usually undesirable and often controlled using symmetry in the system to cancel them out.

A major challenge of designing with CFs is the fact that the stiffnesses can be intrinsically coupled with each of the element parameters. K_z stiffness also decreases rapidly with sweep angle, making K_z more compliant and less of a constraint. This makes adjusting and optimizing parameters more difficult especially with regards to designing around stiffness ratios, whose relationships are plotted in figure 1-5. Varying t_z does not affect z stiffness as much as in straight beam flexures, as shown later. Instead, achieving x - y - θ_z functionality relies mainly on carefully choosing a sweep angle that meets those needs.

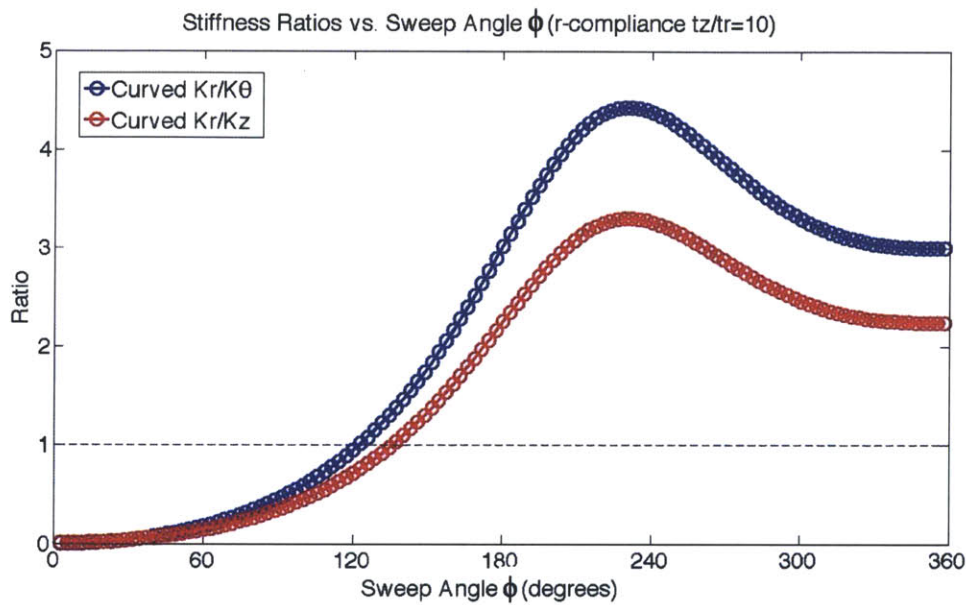


Figure 1-5: Stiffness ratios for an r -compliance flexure element K_r/K_z and K_r/K_θ plotted against sweep angle, ϕ .

1.1.3 Design Rules of CFs

Design rules and mathematical models for straight beam flexures are widely used, but cannot be applied to curved beam CF flexures because of their more complicated geometry and kinematics. Maria Telleria, in her PhD thesis work, determined rules and guidelines for designing curved beam flexures, setting the path for CFs to become more prevalent in precision engineering [5]. Applying these rules in the design of an x - y - θ_z

stage demonstrates their usability, and sets an example for designing with CFs for x-y- θ_z applications. The x-y- θ_z stage design process combines elements in different system configurations, giving rise to additional guidelines for CF design and refining the current ones.

The CF design rules start by modeling the behavior of single CF flexure elements. A CF element can be modeled using a compliance matrix, (1.1), that maps forces to displacements. The compliance matrix is comprised of entries with two components, the usual straight beam equation and a curvature adjustment factor, ζ , building on the familiarity of straight beam flexure design [5].

The equations in (1.4) for the curvature adjustment factor, ζ , show that the curvature adjustment factor depends on two parameters: sweep angle, φ , and the ratio comparing the bending to torsional properties of the beam, β . β is defined in equation (1.2). E is Young's modulus of elasticity, G is the shear modulus, I_z and I_r are the area moments of inertia about the z -axis and r -axis respectively, and k_t , (1.3), is the torsional stiffness constant for a constant cross section. For a rectangular beam, k_t is defined as shown in equation (1.3), where a corresponds to the longer length and b corresponds to the shorter length of the rectangle.

$$[C] = \begin{bmatrix} \zeta_{11} \frac{L^3}{3EI_z} & \zeta_{12} \frac{L^3}{3EI_z} & 0 & 0 & 0 & \zeta_{16} \frac{L^2}{2EI_z} \\ \zeta_{21} \frac{L^3}{3EI_z} & \zeta_{22} \frac{L^3}{3EI_z} & 0 & 0 & 0 & \zeta_{26} \frac{L^2}{2EI_z} \\ 0 & 0 & \zeta_{33} \frac{L^3}{3EI_r} & \zeta_{34} \frac{L^2}{2EI_r} & \zeta_{35} \frac{L^2}{2EI_r} & 0 \\ 0 & 0 & \zeta_{43} \frac{L^2}{2EI_r} & \zeta_{44} \frac{L}{EI_r} & \zeta_{45} \frac{L}{EI_r} & 0 \\ 0 & 0 & \zeta_{53} \frac{L^2}{2EI_z} & \zeta_{54} \frac{L}{EI_z} & \zeta_{55} \frac{L}{EI_z} & 0 \\ \zeta_{61} \frac{L^2}{2EI_z} & \zeta_{62} \frac{L^2}{2EI_z} & 0 & 0 & 0 & \zeta_{66} \frac{L}{EI_z} \end{bmatrix} \quad (1.1)$$

$$\beta = \frac{EI_R}{Gk_t} \quad (1.2)$$

$$k_t = ab^2 \left[\frac{1}{3} - 0.21 \frac{a}{b} \left(1 - \frac{b^4}{12a^4} \right) \right], \text{ for } a \geq b \quad (1.3)$$

$$\zeta_{11} = \frac{3}{\phi^3}(1.5\phi - 2\sin(2\phi) + 0.25\sin(2\phi)) \quad (1.4a)$$

$$\zeta_{12} = \zeta_{21} = \frac{3}{\phi^3}(\cos\phi + (0.5\sin\phi)^2 - 1)) \quad (1.4b)$$

$$\zeta_{16} = \zeta_{61} = \frac{2}{\phi^2}(\phi - \sin\phi) \quad (1.4c)$$

$$\zeta_{22} = \frac{3}{\phi^3}(0.5\phi - 0.25\sin(2\phi)) \quad (1.4d)$$

$$\zeta_{26} = \zeta_{62} = \frac{2}{\phi^2}(\cos\phi - 1) \quad (1.4e)$$

$$\zeta_{33} = \frac{3}{\phi^3}[\phi(1.5\beta + 0.5) - 2\beta\sin\phi + \sin\phi\cos\phi(0.5\beta - 1)] \quad (1.4f)$$

$$\zeta_{34} = \zeta_{43} = \frac{2}{\phi^2}[\beta\sin\phi - 0.5(\beta + 1) + 0.5\sin\phi\cos\phi(1 - \beta)] \quad (1.4g)$$

$$\zeta_{44} = \frac{1}{\phi}[0.5\phi(\beta + 1) + 0.5\sin\phi\cos\phi(\beta - 1)] \quad (1.4h)$$

$$\zeta_{45} = \zeta_{54} = \frac{1}{\phi}[(\beta - 1)0.5\sin^2\phi] \quad (1.4i)$$

$$\zeta_{55} = \zeta_{54} = \frac{1}{\phi}[0.5\phi(\beta + 1) + 0.5\sin\phi\cos\phi(1 - \beta)] \quad (1.4j)$$

$$\zeta_{66} = 2 \quad (1.4k)$$

The next step after determining the behavior of a single CF flexure element is combining multiple elements into a flexure system model. Modeling flexure systems requires an understanding of the boundary conditions imposed on the elements when they are assembled into the system. When combining free CF elements into flexure systems, certain configurations add constraints. The system model accounts for the element boundary conditions by using Gaussian elimination to remove the constrained DOF. After the boundary conditions are applied, the next step is to transform each element compliance matrix into the system coordinates. From there, elements can be combined using parallel and series flexure rules into a flexure system. Figure 1-6 diagrams the CF system design process.

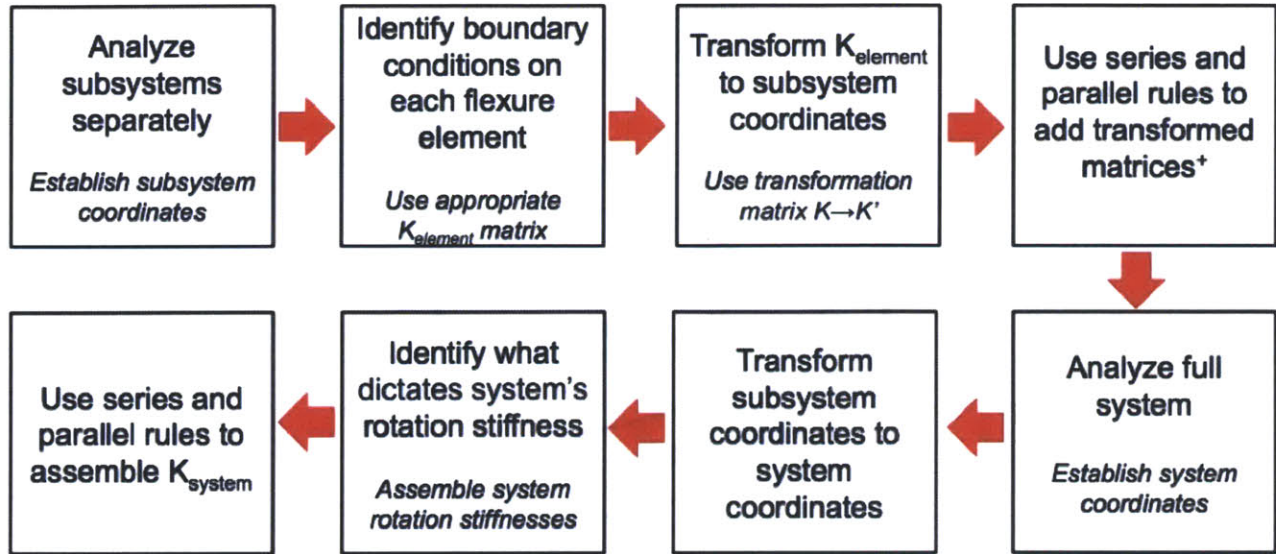


Figure 1-6: Design steps to determine CF system compliance matrix using CF design rules. [5]

1.2 Prior Art in x - y - θ_z Stages

Many examples of The x - y - θ_z stage designs exist, but they typically use straight-beam flexure configurations. A basic x - y - θ_z stage configuration uses, at a minimum, three slender out-of plane beams to support a stage as seen in figure 1-7. The thin beams used are known as wire flexures. They can deflect in both ΔX and ΔY directions due to equally thin dimensions of t_x and t_y . The motions out of plane are constrained, leaving only motion in x , y , and rotation in θ_z . Challenges and trade-offs that arise from this type of straight-beam The x - y - θ_z stage are many, including a limit to the range of motion and beam stiffnesses, unwanted parasitic motions, difficulty in integrating actuators and risk of buckling [2].

Modifications to the basic structure presented by Awatar, allow for better control of the trade offs. One option is adding a fourth element for more stiffness and stability [2]. With flexures and compliant mechanisms, adding another element in parallel does not over constrain the system. Flexure elements can be modeled as springs; when flexure elements in parallel share the same DOF, the system retains that DOF but the stiffness increases.

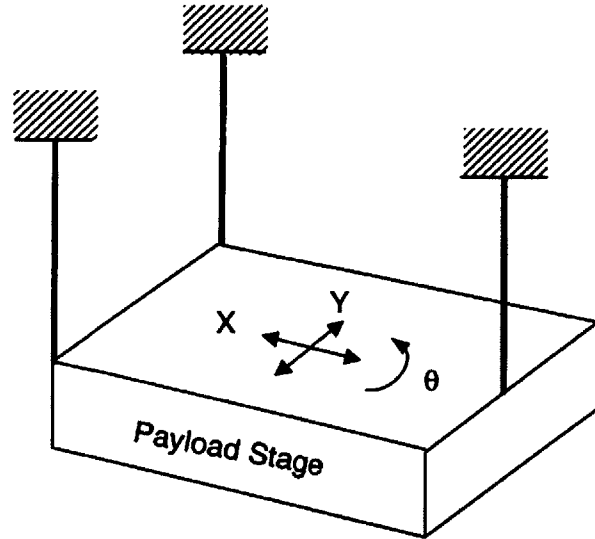


Figure 1-7: Basic straight-beam x-y- θ z stage configuration [2]

Flexures in series, on the other hand, add DOFs, and constrain the system only if they all share the same degree of constraint. A major issue with the basic configuration, which uses a simple four-bar flexure concept, is the unwanted out of plane parasitic motions that arise when the beam deflects. A simple four-bar flexure exhibits an undesired parasitic motion as the flexures bend during deflection. A compound four-bar flexure controls the parasitic motion by adding a second four-bar flexure in series, exploiting symmetry to cancel out unwanted out of plane motion [6]. The parasitic motions in a simple and compound four-bar flexure can be seen in figure 1-8.

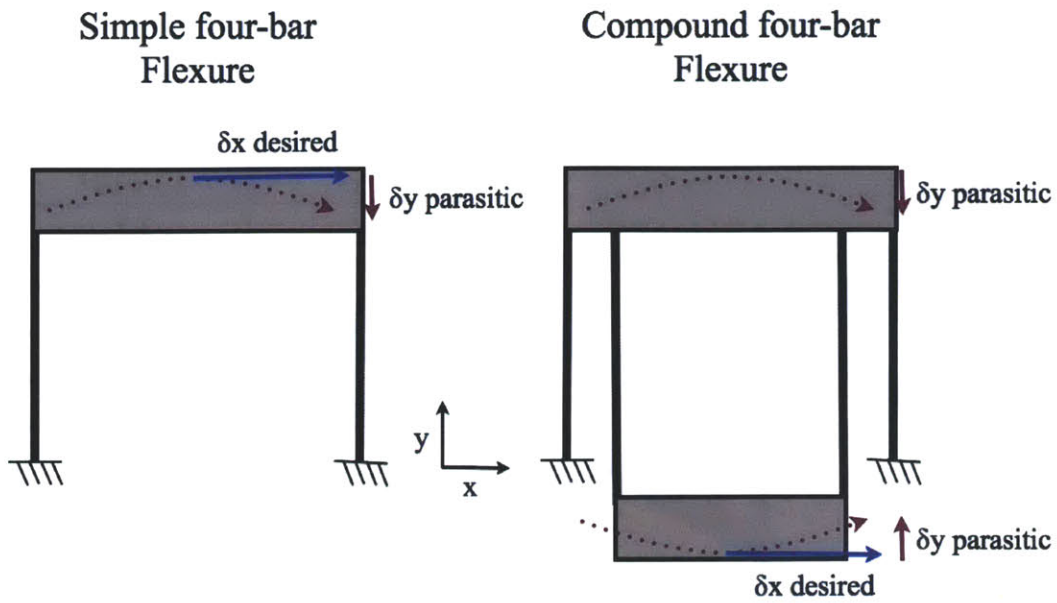


Figure 1-8: A simple four-bar flexure exhibits an undesired parasitic motion. A compound four-bar flexure of two simple four-bar flexures in series exploits symmetry to control unwanted parasitic motion [6].

The compound four-bar configuration of wire flexures was implemented by another student in the PCSL lab in an x - y - θ_z stage design for dip pen nanolithography tip alignment, as shown in figure 1-9 [7]. Figure 1-9 also shows the calculated stiffnesses for the system.

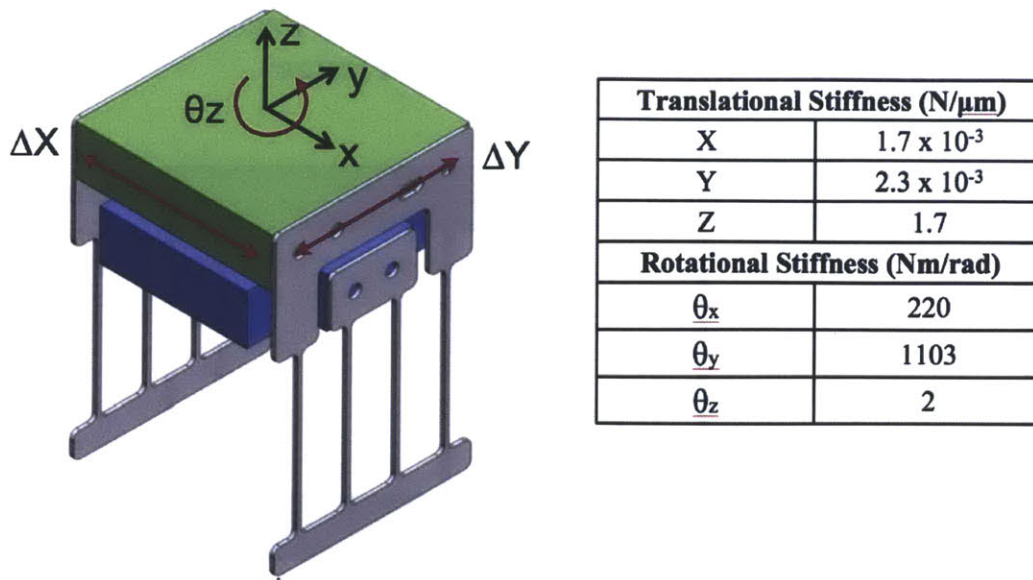


Figure 1-9: A Solidworks model of a straight-beam x-y- θ_z stage using compound four-bar wire flexures and the calculated stiffnesses of the system. [5] [7]

A planar monolithic design for x-y- θ_z motion has been developed by Ryu et. al, using circular single-axis flexure hinge mechanisms and straight-beams for the semiconductor industry [8]. The hinge flexure design is similar to a simpler monolithic design concept that uses three folded hinge flexures in parallel introduced by Hale as seen in figure 1-10a [9]. The folded hinges proved a convenient grounding and actuator attachment points, and the stage is actuated along the triangular axis. The flexure designed by Ryu, et. al. targets tiny displacements with a maximum range of 41.5 μm and 47.8 μm along the X- and Y-axes, and a θ_z rotation of 322.8 arcsec (1.565 mrad) [8]. The design chooses high resolution as a trade off for large range and small footprint. The designers also used mathematical modeling, although specific for a certain configuration, to arrive at the optimized design. The diagram of their piezoelectric actuator driven x-y- θ_z stage can be seen in figure 1-10b [8].

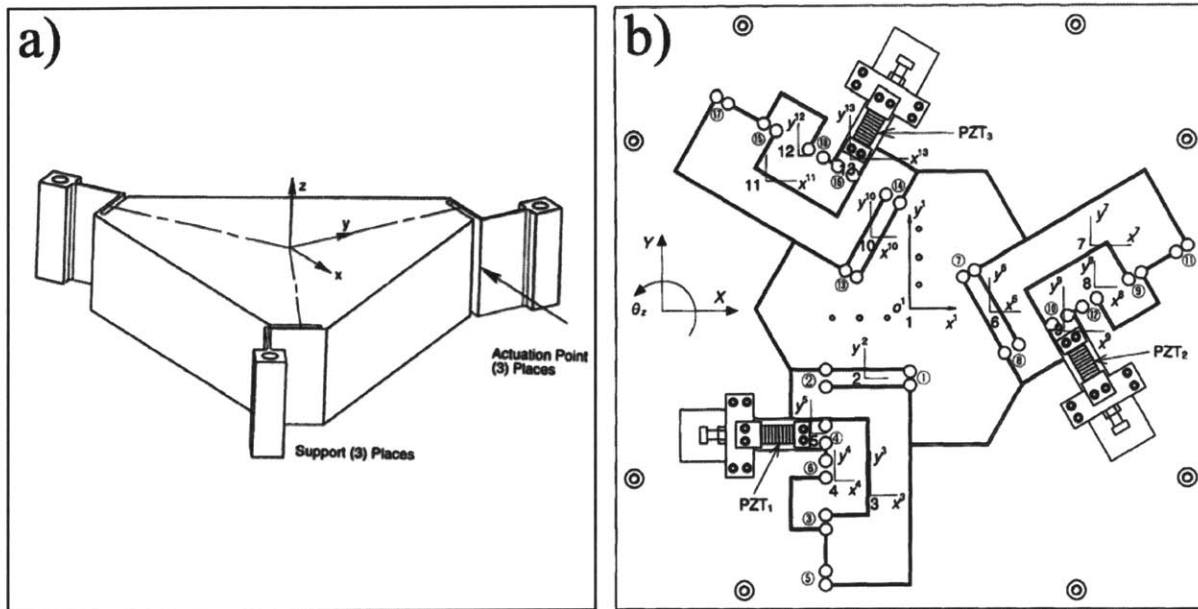


Figure 1-10: a) Folded hinge flexure concept for a x - y - θ_z stage [9] b) Diagram of circular single-axis flexure hinge based design for a x - y - θ_z stage driven by piezoelectric actuators [8]

1.3 Dip Pen Nanolithography

Dip pen nanolithography (DPN) is a nanometer-scale analogy to the quill pen that allows for placement of chemical compounds on solid surfaces. The “nib” is an atomic force microscope (AFM) cantilevered tip, while the desired chemical compound and substrate act as the “ink” and “paper” [10]. DPN has a resolution of as small as 50 nm, but its flexibility allows for the technique to be used to pattern features even as large as 10 microns. DPN is generally an additive process that deposits more material on top of a substrate, but when used with fabrication techniques such as etching or in situ polymerization it can also be subtractive [11]. DPN is a very flexible and fabrication method with uses across many fields. Since its introduction in 1999, DPN has been used for a variety of different functions from generating resists in the semiconductor industry to patterning biomolecular arrays in the biotechnology industry [12]. Figure 1-11 shows the DPN printing process.

A key challenge in DPN is the alignment of the AFM tip with relation to the machine, which needs to be highly accurate and repeatable. Currently the alignment process is

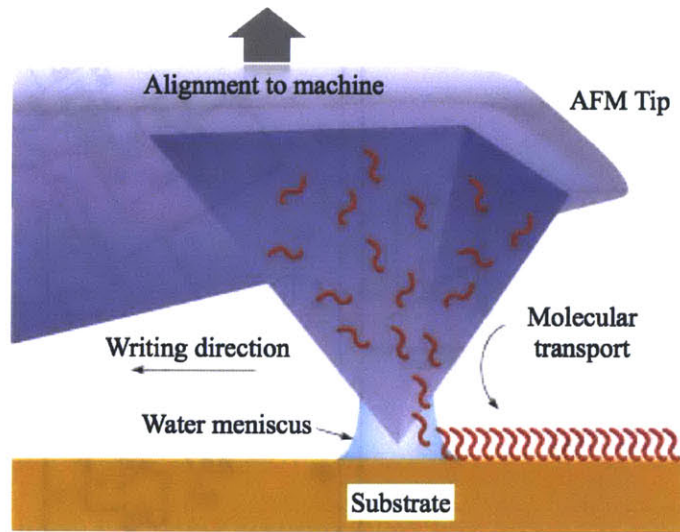


Figure 1-11: Dip pen nanolithography (DPN) schematic representation. An AFM tip is used to convey a liquid chemical compound onto a solid substrate. [13]

manual, so automation would make the process more accurate and less time and labor intensive. While a straight beam flexure system has been previously designed to align and place the tip to the machine [7], the usage of a CF in this application could provide additional benefits regarding space and ease of actuation. Also using the DPN functional requirements to drive the design of a CF flexure system will prove usability of CF design rules and add to the body of knowledge regarding CFs.

Chapter 2

Design

2.1 Design Goals and Functional Requirements

Functional requirements are determined based on the specifications of the actuators, the range of motion required for DPN tip alignment and a factor of safety. Lorenz force linear actuators will be used to position the stage, so the maximum force output should be able to achieve more than the desired amount of displacement. Given a force and a displacement, the desired system stiffnesses can be calculated from Hooke's law.

The flexure corrects the misalignment of the DPN tip, so the alignment error compensation requirements determine the desired ranges of travel for the stage. These ranges are calculated considering variation in tip sizes and machining tolerance. It was found that a translation of 136 microns in both X and Y directions, and a rotation of 0.1 radians, roughly 6 degrees, in theta z are necessary [7]. In case of other errors, a safety factor of 2 is used, so the final functional requirements for displacements are 272 microns of travel in ΔX and ΔY , and 0.2 radians of rotation, 0.1 degrees in each direction.

To actuate the stage, a linear voice coil motor, model number LVCM-013-013-02 from Monticont, will be used. The half-inch diameter voice coil motor supplies a continuous force of 0.81 N and a stroke length of 12.8mm [14]. The maximum stiffness of the flexure for the actuator to execute the required distances would be 3.16 N/mm in the ΔX and ΔY

directions. For the theta rotation, an assumption is made that two linear force actuators would push and pull on opposite sides of the stage with a moment arm of four inches each. In this configuration, the flexure system should have a torsional stiffness of 3371 Nmm/rad or less in θ_z . Other possibilities could be used to actuate the θ_z direction, such as using a motor, to provide a direct moment and greater torque. The constrained directions must also be sufficiently stiff in comparison to the degrees of freedom. Stiffness ratios, K_x/K_z and $K_{\theta_z}/K_{\theta_x}$, should be less than 1/3, and ultimately as low as possible, to ensure that the constrained directions are properly constrained. Table 2.1 outlines the target stiffnesses of the flexure system based on linear actuator capabilities.

Table 2.1: Target DOF stiffnesses and ranges for flexure system driven by the actuator limitations.

Maximum Stiffnesses	Values	Minimum Ranges	Values
K_x	2.98 N/mm	ΔX	6.4mm
K_y	2.98 N/mm	ΔY	6.4mm
K_{θ_z}	3.18 Nm/rad	θ_z	0.4 rad

Another consideration that affects the desired system stiffnesses is the flexure range. The flexure range, the amount of allowable motion before plastic deformation, should have a factor of safety of at least 2 for the required motion, and be beyond the range of the actuators. The range of the flexure is calculated using analytical models for the displacement and stress of the beam and is verified using FEA. Beyond meeting the necessary functional requirements, other design goals included minimizing footprint and volume, as well as developing a monolithic design with little to no assembly, to reduce cost, complexity, and interfaces where slip between surfaces may occur.

2.2 Design Process

The CF system design process is an iterative process, as different ideas were developed to better fulfill the functional requirements of the system. Many different designs were considered and analyzed before the final design was chosen.

2.2.1 Loading Behaviour of a Single r -compliance Flexure Element

Cylindrical flexures have unique loading characteristics, and it is important to understand the resulting motions of a flexure free end tip when designing with them. When loaded in a single direction, motion in the desired direction occurs, as does a parasitic motion in the 90 degrees clockwise direction from actuation and a tip rotation about the z-axis. Figure 2-1. outlines the deflections for a single r -compliance element tip due to different loading conditions. The blue arrows denote the desired motion while the green arrows show the parasitic displacement and the maroon arrows show the parasitic rotations.

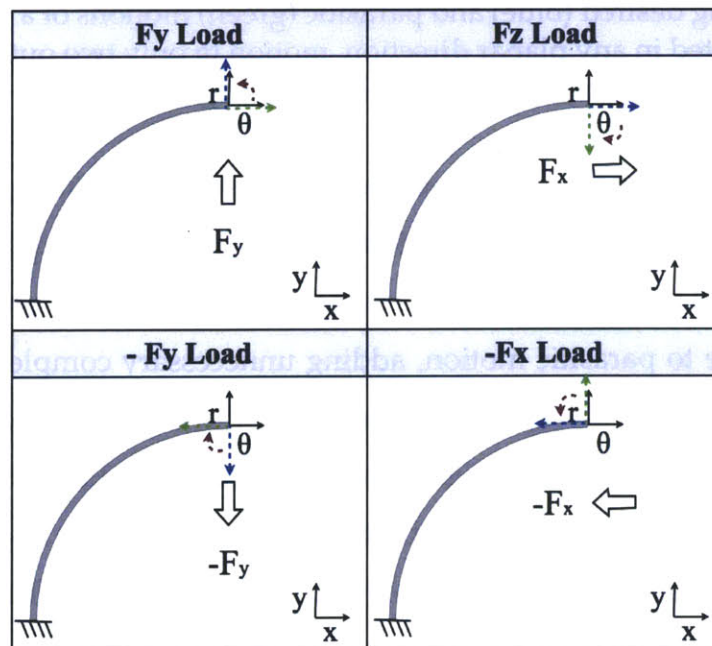


Figure 2-1: Resulting deflections and rotations in a single r -compliance element tip due to different loading conditions. The blue arrows denote the desired displacement while the green and maroon arrows show the parasitic displacement and rotation.

2.2.2 Two, Three, and Four Element Systems

Since the simplest design that achieves a goal is often the best design, the simplest flexure system, a two-element flexure, served as the starting point. This simple system could achieve x - y - θ_z motion, but a motion study of the system showed that it could only attain motion in two quadrants rather than the desired four. As shown in figure 2-2, only motion in the top left and bottom right quadrants result from actuation in any direction. For this reason, the two-flexure configuration was ruled out for an x - y - θ_z stage design.

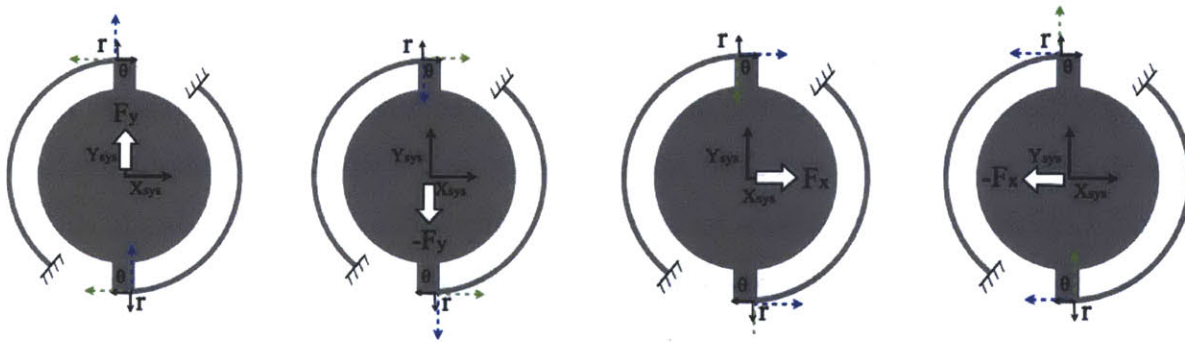


Figure 2-2: Resulting desired (blue) and parasitic (green) motions of a two-flexure system design. When actuated in any planar direction, motion in only two out of the four desired quadrants can be attained, making the two-flexure design unfit for an x - y - θ_z stage

The next idea explored was a three-element flexure, shown in figure 2-3, which unlike the two-flexure system, could provide the motion in all four quadrants. Although the lack of symmetry in the system means that the actuation direction and resulting motion are off axis due to parasitic motion, adding unnecessary complexity to the system. One approach could be to place the actuators along the triangular axis instead of along the stage coordinate system. But designing around unbalanced parasitic motions would limit viable designs and may not be the best configuration to use. Because of the added complexity, more designs were explored beyond the three-element flexure design.

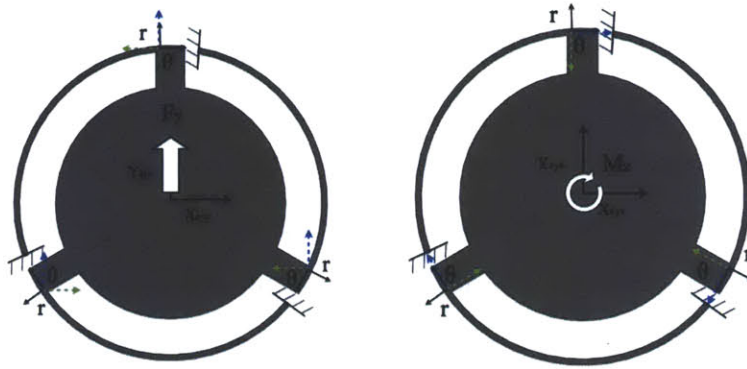


Figure 2-3: Resulting desired (blue) and parasitic (green) motions of a three-flexure system design under F_y and M loads. For the bottom two flexures, the resulting motions are off-axis either to stage coordinate system or to the flexure element coordinate system, adding complexity to the system.

Next, a four-element system with half the elements in opposite directions, as shown in figure 2-4, was considered. Symmetry is restored in a four-element configuration, but shorter length is available to each flexure element, increasing system stiffnesses. In this case, symmetry cancels out the parasitic motion and decouples the X and Y motions. Unfortunately, achieving enough θ_z rotation to meet the desired specifications would be difficult, because the adjacent flexures fight each other in canceling out parasitic motions.

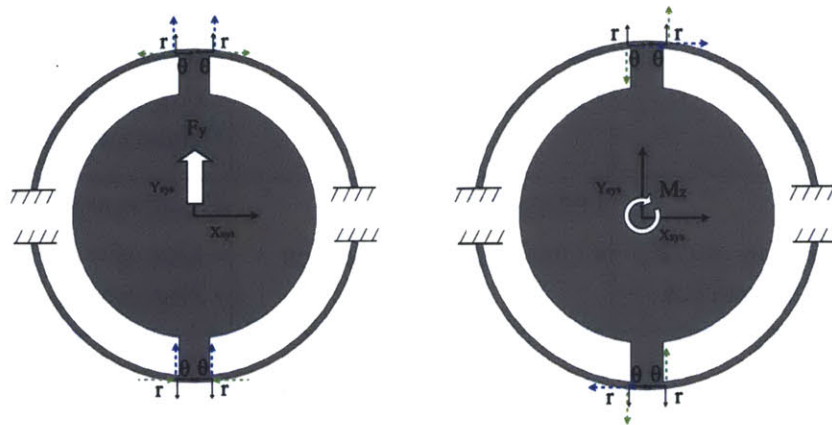


Figure 2-4: Resulting desired (blue) and parasitic (green) motions of a four-flexure system design under F_y and M loads. Symmetry cancels out the parasitic motion and decouples the X and Y motions, but also increases stiffnesses for θ_z .

The summary of the advantages and disadvantages of each of the three designs can be seen in figure 2-5. None of the three have a decisive advantage over the others, although to four-flexure design has the most promising advantages. New designs to be considered should address and remedy the disadvantages in the current four-flexure design. One issue is the increasing stiffness with the addition of more flexure elements, making the four-flexure design the most stiff. As the number of concentric flexures used in the system increases, the sweep angle available for each element decreases. This limits the length of the flexure unless the flexure radius is increased which increases the system footprint. Since a design goal is to minimize footprint, the next iteration of designs utilizes non-concentric flexure elements off axis from the stage.

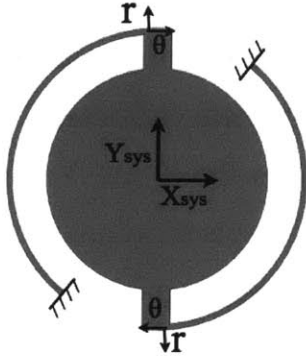
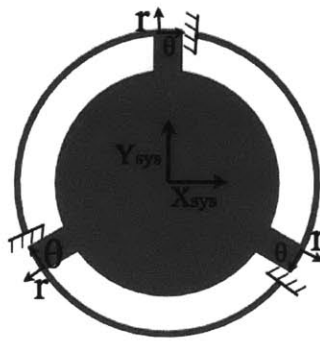
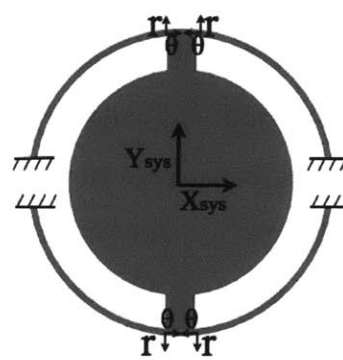
2 Element Concept	3 Element Concept	4 Element Concept
		
<p><u>Advantages:</u></p> <ul style="list-style-type: none"> • Lowest $K_{\theta z}$ • Φ Max 180 	<p><u>Advantages:</u></p> <ul style="list-style-type: none"> • Max $\phi = 120^\circ$ 	<p><u>Advantages:</u></p> <ul style="list-style-type: none"> • Highest $K_{\theta x}$, $K_{\theta y}$ and K_z • Balanced Parasitics
<p><u>Disadvantages:</u></p> <ul style="list-style-type: none"> • Lowest $K_{\theta x}$, $K_{\theta y}$ and K_z • Unbalanced Parasitics 	<p><u>Disadvantages:</u></p> <ul style="list-style-type: none"> • Unbalanced Parasitics 	<p><u>Disadvantages:</u></p> <ul style="list-style-type: none"> • Max $\phi = 90^\circ$ • Highest $K_{\theta z}$

Figure 2-5: A comparison of the advantages and disadvantages of two, three, and four element systems designs. None of the three designs has a decisive advantage over the others [5].

2.2.3 Four-element Off-axis System (Spider Flexure)

From the earlier studies, a four-element flexure was shown to be the best configuration in terms of balancing parasitic motions and having high stiffnesses, K_{θ_x} , K_{θ_y} and K_z , in the desired constraint directions. However the disadvantages of high θ_z stiffness and limited sweep angle available for each flexure needed to be addressed. To reduce the θ_z stiffness, flexure elements are rotated so that they all face the same rotational direction, clockwise from tip to ground. The elements are also moved off axis so they are no longer concentric with the stage, allowing more room for larger sweep angles. Now that the elements are no longer constrained to be concentric to the stage, element sweep angles can be increased to be as great as 270 degrees. The elements attach perpendicularly to the stage opposite each other to provide the symmetry that cancels unwanted parasitic motions. Figure 2-6 shows the configuration of the four-element off-axis system with a sweep angle of 180 degrees.

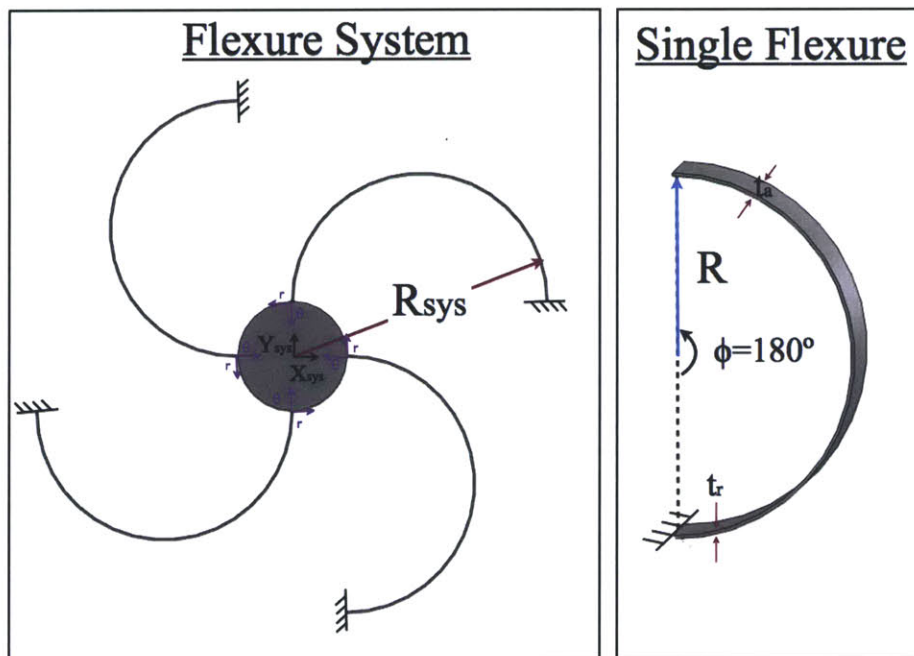


Figure 2-6: Four-element, off-axis System configuration made up of elements with sweep angles of 180 degrees. Parasitic motions are cancelled out

Applying CF design rules helped determine the optimal sweep angle and radii for each element. In this configuration, the element stiffnesses relate to the overall system stiffnesses, as shown by equations (2.1 - 2.4).

$$K_{x-sys} = K_{y-sys} = 2K_{r-element} + 2K_{\theta-element} \quad (2.1)$$

$$K_{z-sys} = 4K_{z-element} \quad (2.2)$$

$$K_{\theta z-sys} = 4K_{r-element} * r_{stage}^2 \quad (2.3)$$

$$K_{\theta z-sys} \approx K_{\theta y-sys} = 2K_{z-element} * r_{stage}^2 \quad (2.4)$$

The radius of each element is constrained by the total footprint. A radius of 3 inches was chosen for the total system and a stage radius of 0.5 inches. It was found that with the corresponding element radius, an element sweep angle greater than 180 degrees would be needed to achieve the desired stiffnesses as well as to minimize the unwanted parasitic motions. This is illustrated in figure 2-7 which plots the normalized stiffnesses of the system in the r and θ direction.

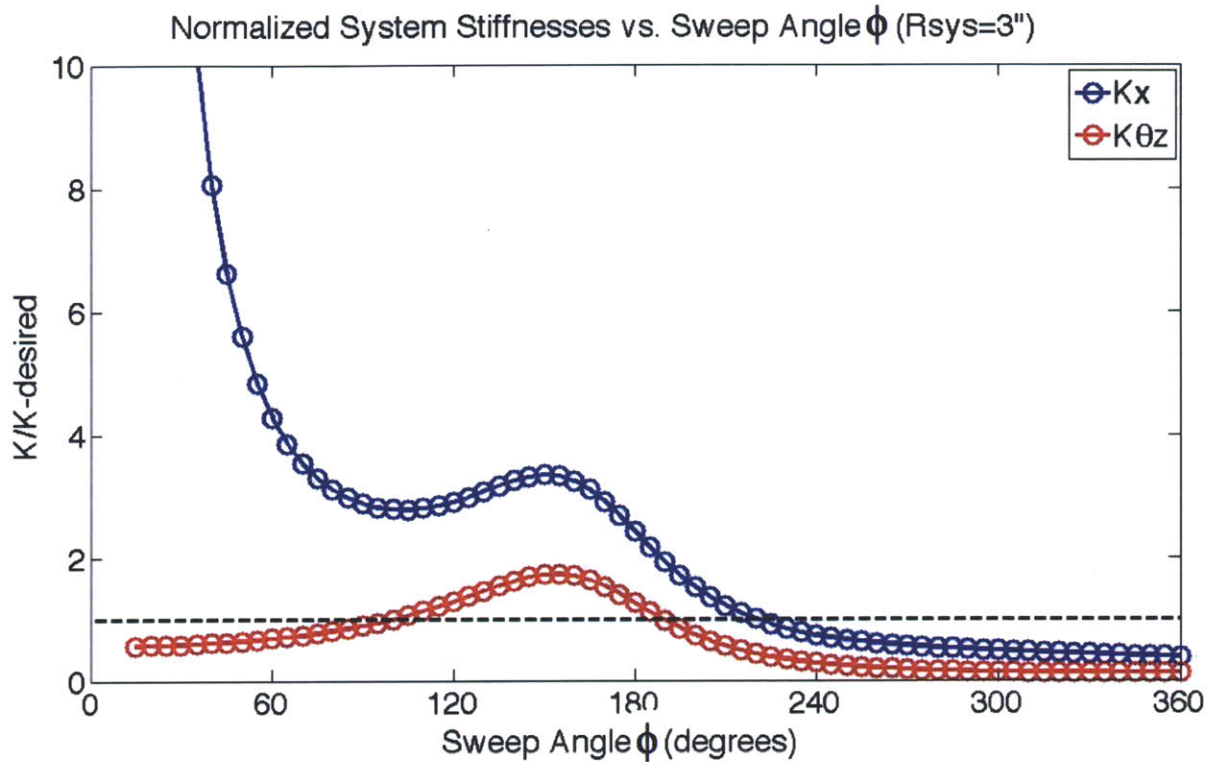


Figure 2-7: Four-element off-axis system in-plane, normalized stiffnesses vs. element sweep angle, ϕ . Desired stiffnesses occur at sweep angles of greater than 180 degrees. (K_x desired = 1700N/m, K_{θ_z} desired = 2Nm/rad, $R_{sys} = 3$ in, $R_{stage} = 0.5$ in, $t_z = 0.5$ in, $t_r = 0.024$ in, 6061-T6 Al)

To save space, an attachment angle η can be introduced as shown in figure 2-8. An attachment angle allows for the element radii to be increased while keeping the same overall system radius since flexures can be more tightly packed. An attachment angle also creates a rotation of all the flexures that results in θ_z stage actuation aligning more along the element θ directions rather than element r directions. For large sweep angles, K_θ is less than K_r , so a larger attachment angle η lowers the overall K_{θ_z} for the system, an additional benefit of adding an attachment angle.

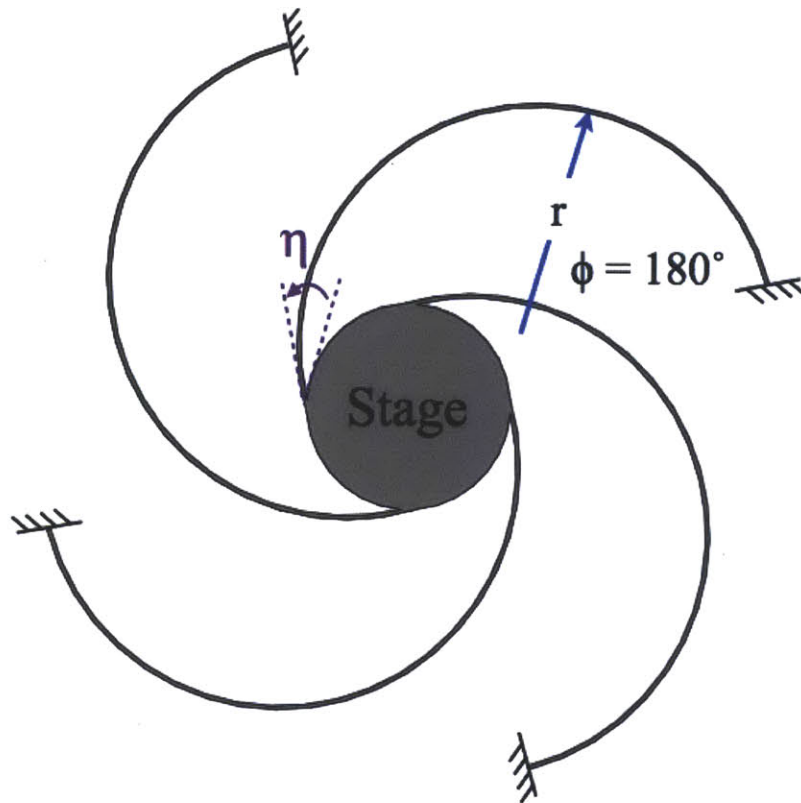


Figure 2-8: Four-element Off-axis System with added attachment angle, η .

While the four-element off-axis system successfully achieves the desired stiffnesses in a sufficiently small footprint with sweep angles greater than 180 degrees, the stiffness ratios when compared to the constrained directions are much too high. Figure 2-9 depicts the spider flexure system stiffness ratios versus the element sweep angle ϕ .

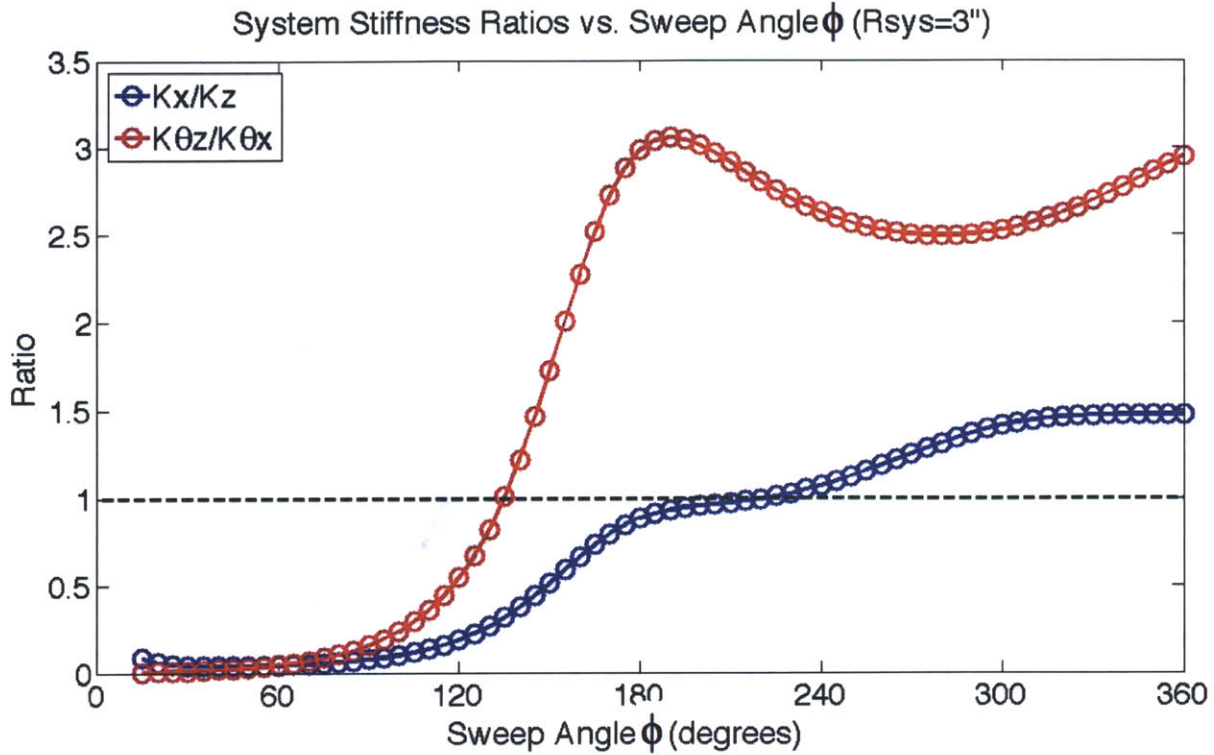


Figure 2-9: Four-element off-axis system stiffness ratios vs. element sweep angle, ϕ . The stiffness ratios at 180 degrees and greater are undesirably high. ($R_{sys} = 3$ in, $R_{stage} = 0.5$ in, $t_z = 0.5$ in, $t_r = 0.024$ in, 6061-T6 Al)

An optimized design of the system resulted in stiffness ratios barely constraining ΔZ and θ_x and θ_y . Smaller sweep angles at around 60 degrees would attain better stiffness ratios, but large sweep angles are required to achieve desired stiffnesses as shown earlier. As larger element sweep angles are used, the stiffness in the ΔZ direction no longer cubically increases with depth, t_z , as in the case of straight beams. This results from twisting out of plane in the flexure element, rather than bending, as demonstrated in figure 2-10. Increasing t_z has a large effect on bending but little effect on twist, so its effect is significantly lower than in straight beams.

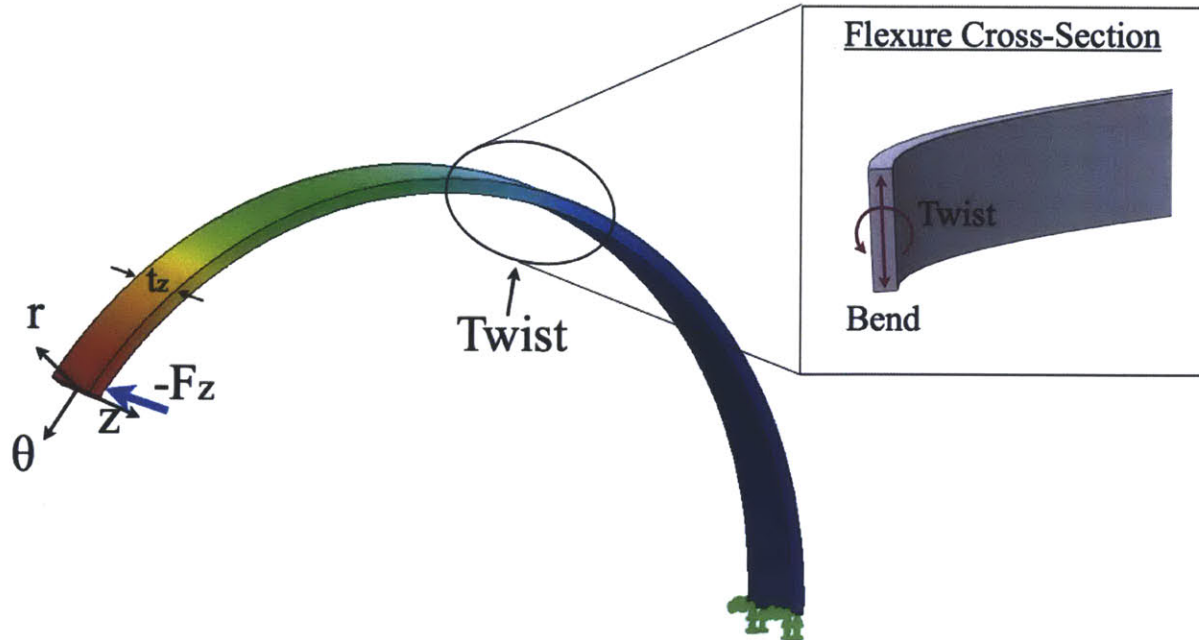


Figure 2-10: FEA of a single CF element with large sweep angle shows twist in ΔZ which makes system less stiff compared to a straight-beam flexure with similar z thickness.

This design acts more like a 6 DOF stage rather than an x - y - θ_z stage, and with a few adjustments, perhaps this design could be used as such. But in the design for an x - y - θ_z stage that meets the functional requirements outlined earlier, another design needed to be considered.

2.2.4 Serial Four-element System (Serial Spider Flexure)

From figure 2-9, smaller sweep angles achieve better stiffness ratios than larger sweep angles. Unfortunately, as seen in figure 2-7, the stiffnesses at lower sweep angles are much too stiff to meet functional requirements. Meeting the design goals requires the stiffness of an element with a 180 degree sweep angle or greater, but the stiffness ratios analysis indicates that the sweep angle must be less than 90 degrees. To resolve this contradiction, two 60 degree elements in series are used in place of the 180 degree single element. Flexures in series add according to equation (2.5), so the stiffness of two 60 degree flexures in series is half that of a single one. Since all stiffnesses decrease proportionally, we still

retain the desired stiffness ratios.

$$k_{eq} = \frac{1}{\sum_{i=1}^n \frac{1}{K_i}} \quad (2.5)$$

One arrangement for placing the elements in series would be a double decker design, illustrated in figure 2-11. In this case, the two layers would each be fabricated monolithically, and the intermediate stages would be connected together. This introduces risks such as errors and tolerances in assembly, but can be beneficial if footprint size is constrained and depth is not of concern.

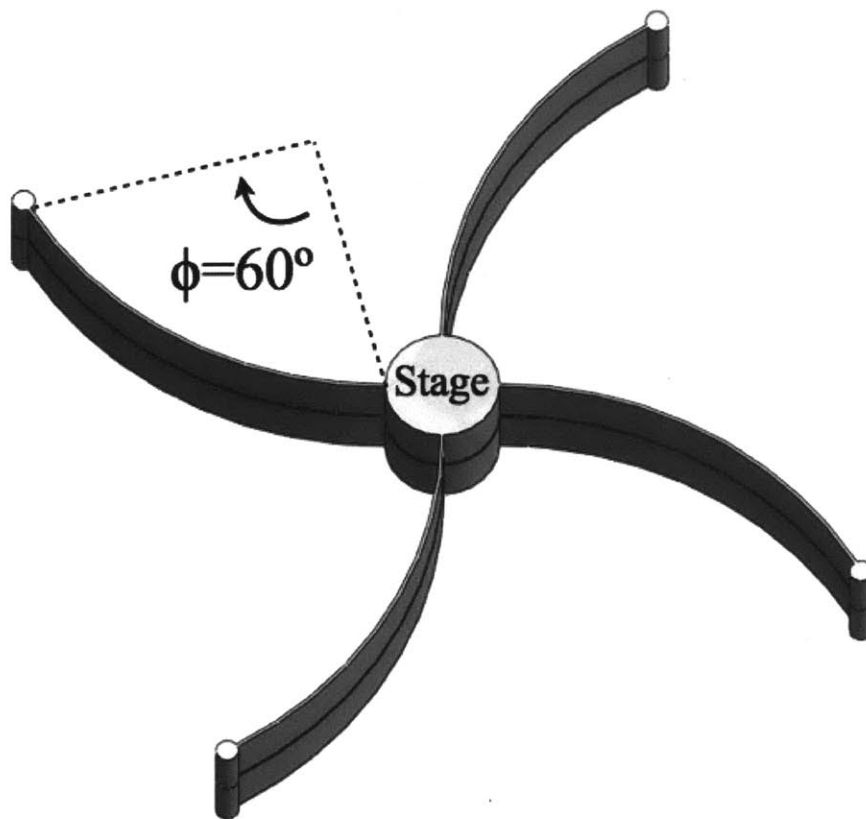


Figure 2-11: Double decker system design with two 60-degree elements in series to replace the single 180 degree flexure arm used previously.

For this work, monolithic fabrication with no assembly is a key design goal. If a flex-

ure attachment angle, ν , is introduced at the junction between the two flexures in series, then the entire flexure system could remain on a single plane. The effects of an attachment angle could even help in increasing the stiffness ratios, and provide yet another design variable that can be adjusted. Figure 2-12 shows the new serial four-element design with series attachment angles, ν , and stage attachment angle η , that serve as additional adjustments.

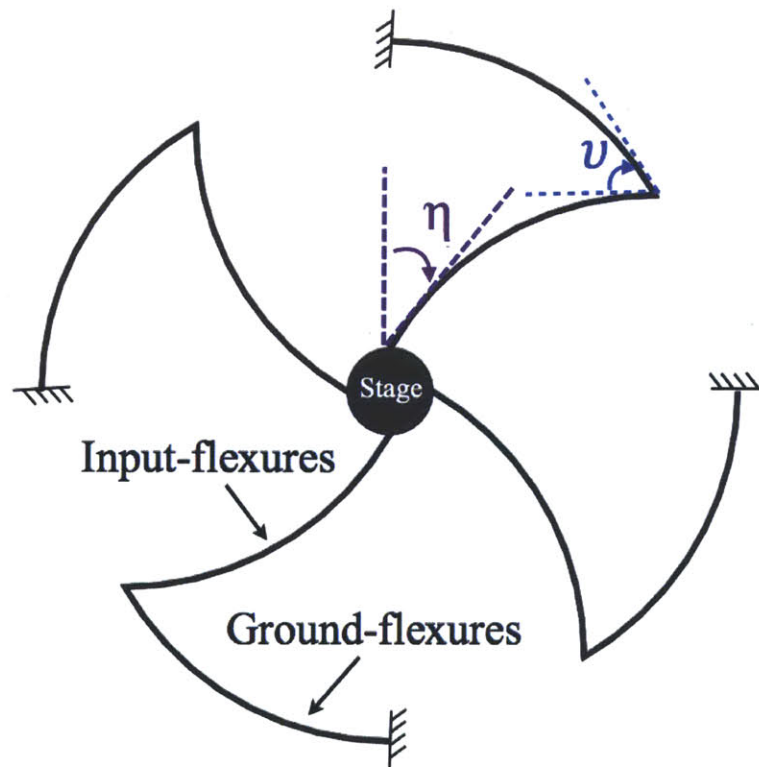


Figure 2-12: Four two-series element systems with stage attachment angle, η , and series attachment angle, ν , to help with stiffness ratios and monolithic machinability.

2.3 Final Design - Concept Optimization and Verification

The serial four-element system with an intermediate flexure proved to be the best design to reach the design goals outlined at the beginning. Using the CF rules and system model, the optimal values for η , ν , and element radii were determined. An FEA model was then created to corroborate the calculations from the model. Lastly, the flexure was fabricated and the stiffnesses measured to verify the design.

2.3.1 System Model [5]

Introducing the additional flexure attachment angle, ν , adds yet another transformation matrix to convert the ground flexure tip reference frame to the input flexure reference frame. The transformation matrix can be seen in equations (2.6 - 2.7). Adding those equations into the model demonstrates how the attachment angles affect functional requirements.

$$[R] = \begin{bmatrix} -\cos(\phi + \nu) & -\sin(\phi + \nu) & -R(1 - \cos\phi) \\ -\sin(\phi + \nu) & \cos(\phi + \nu) & R\sin\phi \\ 0 & 0 & -1 \end{bmatrix} \quad (2.6)$$

$$[C_t] = [R][C][R]^T \quad (2.7)$$

From there, the flexures can be optimized to find the best parameters to meet the necessary compliance in x and y while still having sufficiently low stiffness ratios to ensure the correct DOFs and constraints. From the plot in figure 2-13, it is determined that a larger series attachment angle, ν , lowers the stiffness in K_{θ_z} while retaining the same stiffness ratios. For that reason, a series attachment angle of 60 degrees is chosen since it is the largest attachment angle allowed without changing the system radius. The final specifications of x-y- θ_z stage design as determined using the model are included in table 2.2.

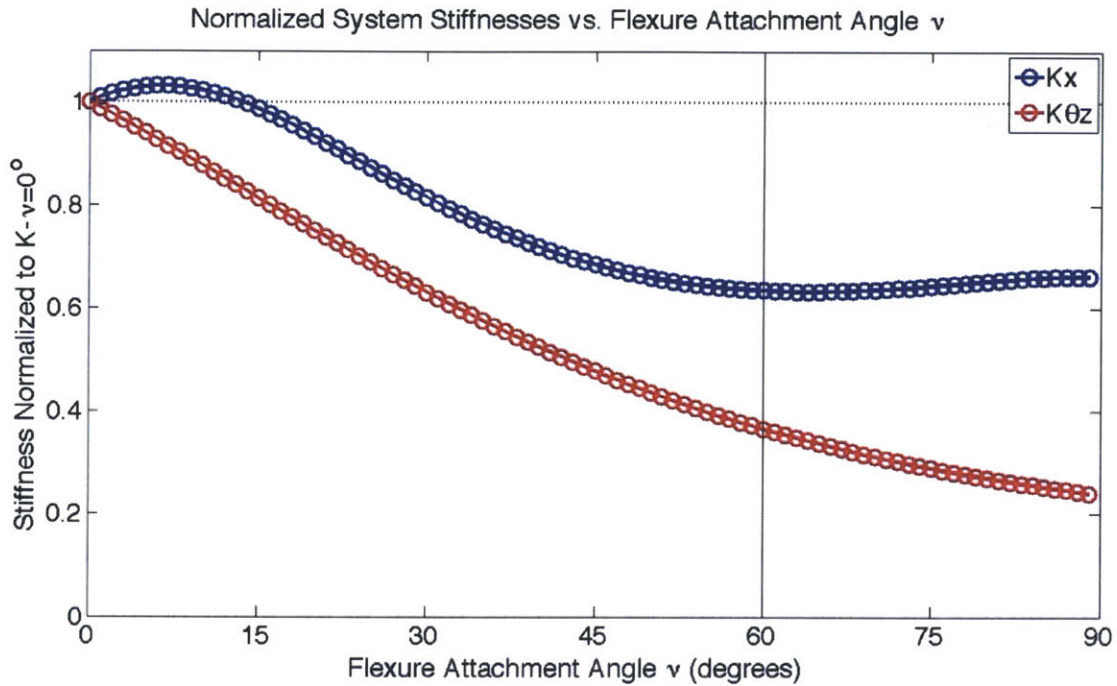


Figure 2-13: Normalized Serial Four-element system stiffnesses vs. flexure attachment angle, ν . ν lowers system stiffnesses in x and in θ_z , but is limited to be less than or equal to 60 degrees in order to not alter R_{sys} . ($\varphi=60$ deg, $R_{sys} = 3$ in, $R_{stage} = 0.5$ in, $t_z = 0.5$ in, $t_r = 0.024$ in, 6061-T6 Al)

This entire design process demonstrates the usability of the models and rules in determining key designs and flexure parameters. The CF models allow for the optimization process to be much faster than using pure FEA modeling. For example, it is known from the model that changing the z -thickness would have a small effect on the performance, unlike in straight-beams where it would have a large effect, and so designers should not waste time varying that parameter. The analytical models give the designer an understanding of the effect of different parameters on the performance of the system. They can be used to quickly analyze the effect of parameters such as sweep angle, t_z , η , ν and optimize the design to meet the functional requirements.

Table 2.2: Final specifications for CF x - y - θ_z stage element and system parameters

Parameter	Values
Elemental radial thickness, t_r	0.024 inches
System z-thickness, t_z	0.5 inches
System radius, r_{sys}	4 inches
Stage radius, R_{stage}	0.5 inches
Element sweep angle, φ	60°
Stage attachment angle η	0°
Flexure (Series) attachment angle, ν	60°
Material	6061-T6 Al

2.3.2 Modal Analysis

While the directions with lowest stiffnesses are traditionally considered degrees of freedom, using the lowest natural frequency modes can be another way of defining them degrees of freedom. Since it is difficult to compare rotational stiffnesses to linear stiffnesses, modal analysis finds the lowest natural frequency modes allowing a way to compare linear and rotational motions. Modal analysis of the design showed that the first two natural frequency modes of the current design are in ΔX and Y as expected, but the Δz direction has a lower natural frequency than the θ_z , which is undesirable. By placing mass further away from the center of the stage, the natural frequency of motion in θ_z lowers, essentially a flywheel effect. In the fabricated design, four arms are added to the center of the stage. This can be further optimized by placing even more weight as far from the center of the stage as possible by added masses to the end of the four arms. Figure 2-14 summarizes the lowest five natural frequency modes of the three designs.

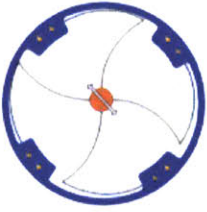
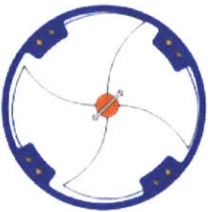


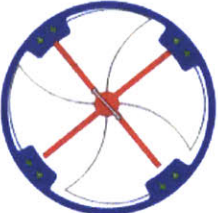
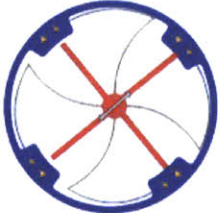
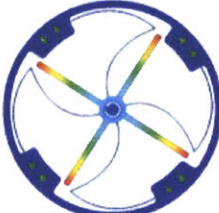



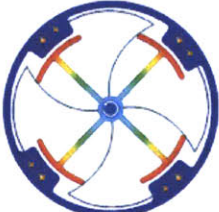

Original Design			
1st Mode	2nd Mode	3rd Mode	4th Mode
			
26.7 Hz	26.80 Hz	80.70 Hz	123.75 Hz
Four Arms Added			
1st Mode	2nd Mode	3rd Mode	4th Mode
			
15.05 Hz	15.09 Hz	24.36 Hz	43.00 Hz
Four Arms with Weights Added			
1st Mode	2nd Mode	3rd Mode	4th Mode
			
12.12 Hz	12.14 Hz	14.62 Hz	34.47 Hz

Figure 2-14: The first four frequency modes for CF Stage with the original design, four arms added, and arms with weights added.

2.3.3 Finite Element Analysis Corroborations

Finite element analysis (FEA) was used to verify the predicted system stiffnesses and stiffness ratios from the model. Having a CF model allowed for optimizing the desired parameters and driving the design without FEA. This saved much time compared to optimizing through FEA, where the designer does not know the effect of the different parameters leading to blind optimization. The analytical models reduced the number of FEA runs that were necessary. For the FEA verification, a fine mesh was used for the thin flexure beams, ensuring that at least three mesh elements spanned across the smallest dimension, t_r . The FEA mesh can be seen in figure 2-15. In each direction, stiffnesses were found by applying a given force or moment on the stage and measuring the distance displaced. For the torsional stiffnesses, simple trigonometry can be used to convert the measured displacements to radians.

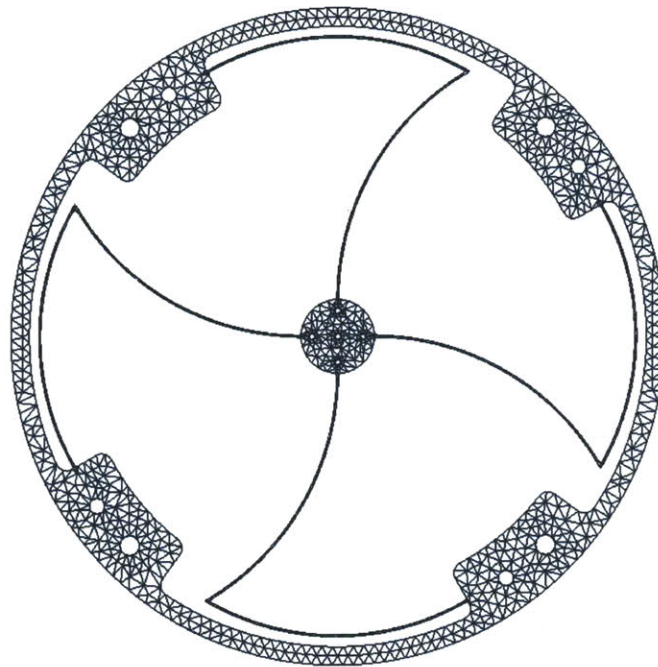


Figure 2-15: FEA mesh of final flexure design. FEA was used to corroborate CF model results.

Table 2.3 compares the stiffness values of the FEA model with the mathematical model. The table shows that the FEA data are similar to, but are slightly higher than, the stiffnesses calculated by the model. This difference is to be expected because the model generalizes some aspects of the flexure to make it easier to analyze mathematically. The FEA can better capture the more complicated phenomena that the model oversimplifies.

Table 2.3: Stiffness values determined by model and FEA calculations

Stiffnesses	Model Value	FEA Value
K_x	0.644 N/mm	0.612 N/mm
K_y	0.644 N/mm	0.612 N/mm
K_{θ_z}	2.09 Nm/rad	2.85 Nm/rad

FEA also helps with verifying that the flexure range well encompasses the necessary travel distances. This is verified by assuming a linear relationship between stress, which holds true in the elastic range, and strain, and comparing the stress in the beams to the material's yield stress. The region of highest stress in the system occurs in the input-flexures, the flexures attached to the stage. Using equation (2.8), a factor of safety of 60 is calculated before the flexures yield. In this case, the desired displacements are very small and are well within the elastic region of the flexures with a large factor of safety. The predicted FEA ranges can be seen in table 4.2.

$$\sigma_{yield} \cdot \Delta_{yield} = \sigma_{measured} \cdot \Delta_{measured} \quad (2.8)$$

When compared with the previously designed straight beam flexure, as seen in table 2.5, the CF design attains similar performance for stiffnesses but have much higher stiffness ratios. With CFs, it is possible to fulfill the functional requirements and design goals for a limited footprint and monolithic fabrication. Although the higher stiffness ratios suggest that CFs may be better suited for 6 DOF system designs.

Table 2.4: FEA predictions for range in the three desired directions.

Direction	Range Functional Requirement	Range FEA Prediction
ΔX	$\pm 272 \mu\text{m}$	$\pm 17.53 \text{ mm}$
ΔY	$\pm 272 \mu\text{m}$	$\pm 17.53 \text{ mm}$
θ_z	$\pm 0.2 \text{ rad}$	$\pm 0.26 \text{ rad}$

Table 2.5: FEA calculations of the final CF flexure versus previous straight beam design straight beam [5] [7].

Attribute (required)	Straight-beam flexure (FEA)	CF Design (FEA)
K_x	1.7 N/mm	0.612 N/mm
K_y	2.3 N/mm	0.612 N/mm
K_{θ_z}	2 Nm/rad	2.85 Nm/rad
K_x / K_z	1.0×10^{-3}	1.7×10^{-1}
K_y / K_z	1.4×10^{-3}	1.7×10^{-1}
$K_{\theta_z} / K_{\theta_x}$	9.1×10^{-3}	1.3×10^{-1}
$K_{\theta_z} / K_{\theta_y}$	1.8×10^{-3}	1.3×10^{-1}
ΔX -range ($\pm 272 \mu\text{m}$)	$\pm 5.99 \text{ mm}$	$\pm 17.53 \text{ mm}$
ΔY -range ($\pm 272 \mu\text{m}$)	$\pm 4.18 \text{ mm}$	$\pm 17.53 \text{ mm}$
θ_z -range ($\pm 0.2 \text{ rad}$)	$\pm 0.37 \text{ rad}$	$\pm 0.26 \text{ rad}$
ΔX -range/L	0.079	0.078
Volume	$5.1 \times 5.3 \times 7.6 \text{ cm}$ (205 cm ³)	$22.6 \times 22.6 \times 1.27 \text{ cm}$ (666 cm ³)

2.3.4 Fabrication

The final design was 3D modeled using SolidWorks and fabricated using an OMAX precision abrasive waterjet cutting machine. Waterjet machining is beneficial because it can machine the entire flexure in one pass relatively quickly and also places low load on the flexures. Undesireably, waterjet machining also introduces errors such as a taper angle, and a kerf width, which affects the critical thickness, t_r , of the flexure elements. The flexure was made using fine grit garnet abrasive in the with a level five quality setting, the slowest speed for the smoothest cut.

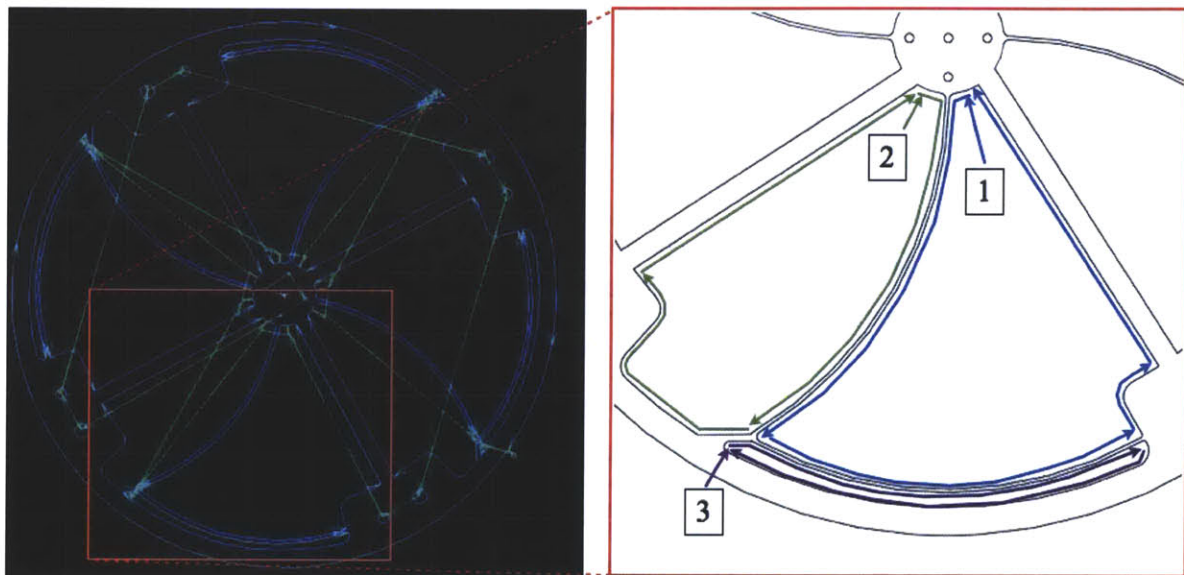


Figure 2-16: OMAX Waterjet machine path figure. The stage and flexures are constrained, and the flexure paths were cut first to minimize cutting error from vibration. The numbers denote the starting points and cutting order for the loops required for each flexure.

Machine cutting path is also critical to result in good flexures. When cutting flexure elements, it is important to constrain the stage during cutting to minimize vibrations which lead to error in the cut. Tabs connecting the main stage and the flexure attachment to the grounding circle, were added as constraints. The order of cut also matters. The critical flexure edges must be cut first before the free pieces can vibrate and also contribute variation to the cut. Manually removing the cut negative parts as they are freed

is also necessary so they do not continue to rattle around and damage the flexures. After an initial failure in machining, in which the flexure was cut through, the thickness of the flexures were increased by 0.006 inches to ensure successful fabrication. Figure 2-16 shows the tabs added to constrain the stages and the flexures, as well as the cutting path that was followed to achieve successful cutting.

After flexure fabrication, measurements of the flexure thicknesses and taper angles were taken. The average flexure thickness was 0.0289 inches with a taper angle of about 0.36 degrees. The fabricated flexures are thicker than the original design, so measured system stiffnesses are expected to be higher than the calculated values from the model.

Chapter 3

Measurement and Testing

3.1 Measurement and Apparatus Design

Once the flexure was fabricated, the measurements were taken to verify the flexure stiffnesses and parasitic motions. The measurement set-up fixes the flexure to an optical table and allows for measurement instrumentation. A system of weights and pulleys were designed to actuate the flexure with a known force, while capacitance probes (cap probes) were used to measure the resulting displacements. Once the force and displacements are known, the stiffnesses of the flexure system can be determined.

Figure 3-1 shows a CAD model of the measurement test set up. A top measurement plate, placed above the flexure, provides fixturing for the capacitance probes and pulleys. The measurement plate was also fabricated using a waterjet to ensure alignment with the flexure. All six capacitance probes attachment points are connected to the measurement plate. Three are located at the top to measure rotation in θ_x and θ_y as well as a displacement in z , two are on the side to measure θ_z and ΔY , and one is on the side to measure ΔX . Two upper pulleys located on the top of the measurement plate actuate the upper portions of θ_x and θ_y . Their counterparts are weights hung underneath the stage to actuate the lower portions θ_x and θ_y . The two create a moment about the x and y axis with a moment arm of 0.35 inches. The measurement set-up raises the flexure above the optical

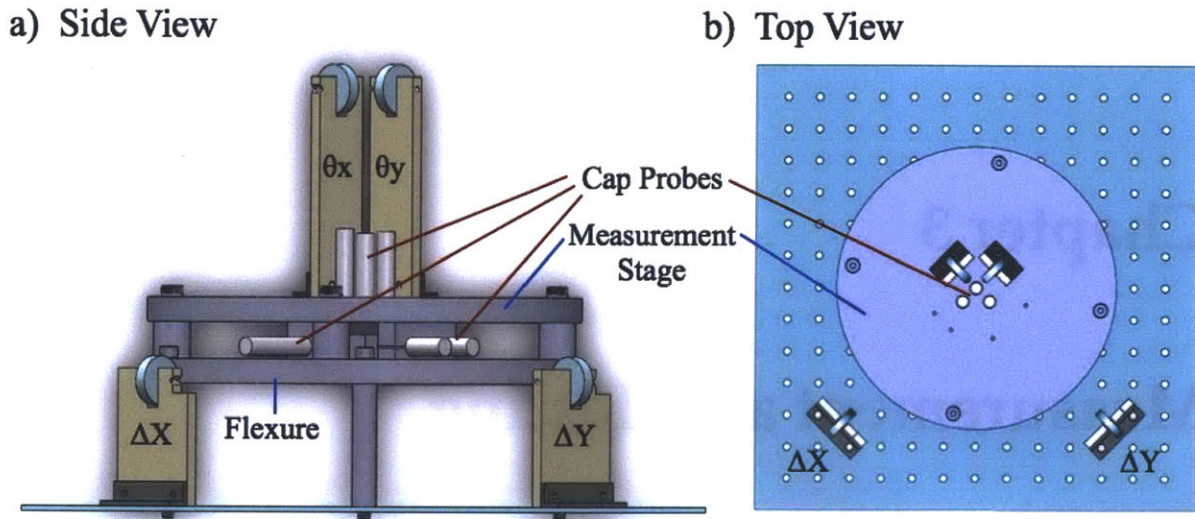


Figure 3-1: CAD model of measurement set up to verify flexure stiffnesses and functionality. Pulleys and weights are used to actuate the stage in a known direction with a given force

table, leaving clearance for weights to be hung underneath. Additional pulleys are fixed to the optical table. These pulleys actuate the stage in ΔX , ΔY and θ_z .

Affixed to the stage of the flexure is a measurement stage. This simulates the load that the stage would hold, and provides a measurement platform for the capacitance probes. The measurement stage also provides a moment arm of 5 inches for the application of a θ_z moment.

3.2 Test Set-up and Measurement Techniques

Capacitance probes were used in conjunction with National Instrument's LabView to record data. The capacitance probes had a conversion of 12.5 micrometer per volt with a range of 250 micrometers. For this set up, the probes were set as close to zero as possible so it could measure displacements of ± 125 micrometers. Exact zeroing is not as critical because only the change in displacement is needed, but the capacitance probes must

encompass the displacements in its measurable range.

To actuate the displacements, weights were chosen to be within measurable range of the capacitance probes and within the range, below yield stress, of the flexure. 10g weights were used to actuate ΔX and ΔY and θ_z , 20 g weights were used to actuate ΔZ , and 50 g weights each were used for actuation in θ_x and θ_y . This translates to a linear force of 0.0981N in the ΔX and Y direction and 0.1962 N in the ΔZ direction and a torsional moment of 12.48 Nmm in θ_z , 8.72 Nmm in θ_x and θ_y . These values are summarized in table 3.1, and a photo of the test set up can be seen in figure 3-2.

Table 3.1: Summary of actuation forces used for measuring stiffness.

Actuation Direction	Weight	Force/Moment Applied
ΔX	0.01 kg	0.0981 N
ΔY	0.01 kg	0.0981 N
Δz	0.02 kg	0.1962 N
θ_x	0.05 kg	8.72 Nmm
θ_y	0.05 kg	8.72 Nmm
θ_z	0.01 kg	12.46 Nmm

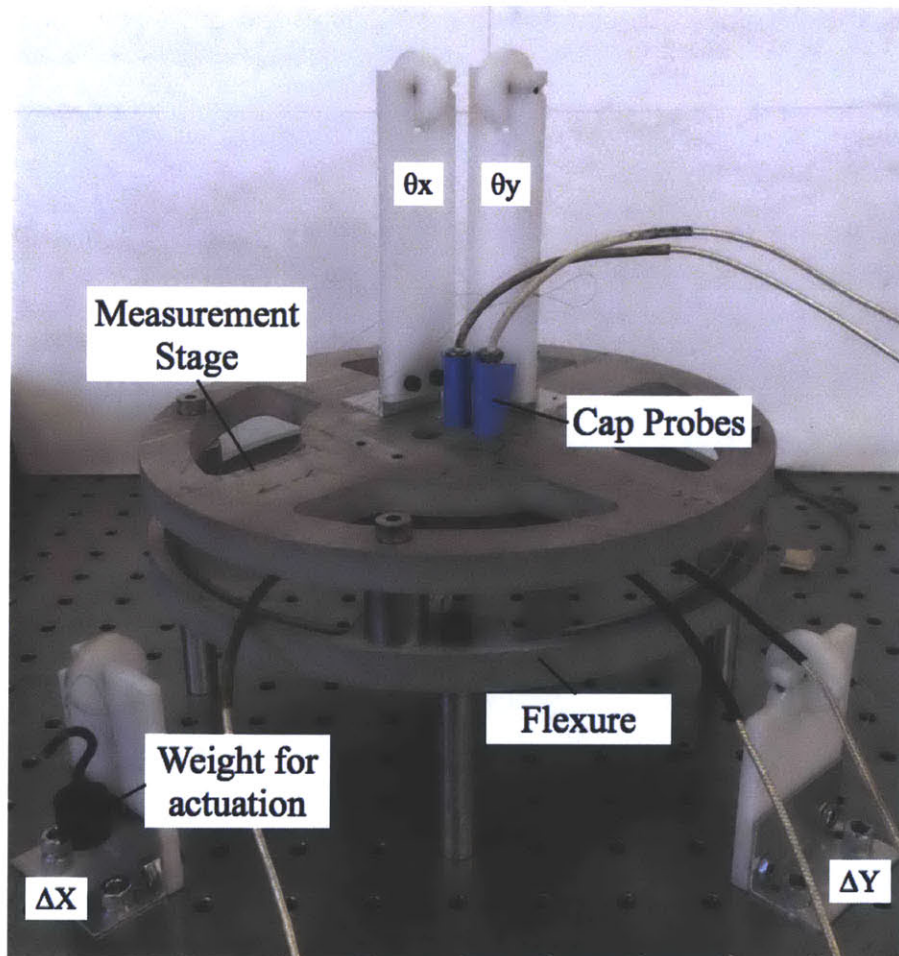


Figure 3-2: Photo of measurement test set up on optical table

Chapter 4

Results and Analysis

4.1 Measured Values Compared to FEA and Model Values

The measured stiffnesses were slightly higher than the original design. This is most likely because the critical thickness of the flexures was increased to 0.03 inches to ensure successful fabrication, but the increase in thickness also increased the stiffnesses. The waterjet fabrication method also introduces a taper angle, making the flexure thicker at the bottom and thinner at the top. It was previously measured and found that the average flexure thickness was 0.0289 inches with a taper angle of about 0.36 degrees. These dimensions were used for a new FEA model (figure 4-1) that accounts for these changes, and indeed the stiffnesses do increase from the original design, as summarized in Table 4.1.

The model allowed for quick optimization of the design parameters, allowing FEA to be a corroboration tool to save time. The model makes a few assumptions to simplify and expedite the math calculations, and an FEA study can verify any discrepancies and catch phenomena that are not as easily modeled. Table 4.1 compares the stiffnesses as predicted by the model, the initial FEA, and the updated FEA, to the measured stiffnesses of the fabricated flexure. They are all within an order of magnitude of each other. The error between the model determined by CF rules and the actual measured values were

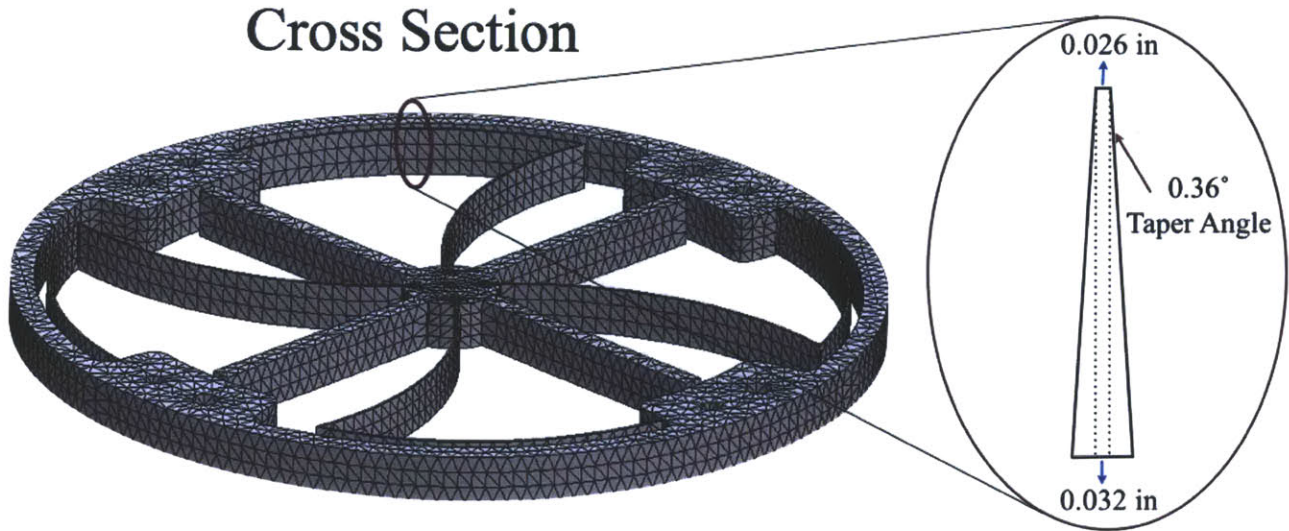


Figure 4-1: FEA analysis on updated model that reflects real machined thicknesses and taper angle. Cross section of one element shows the average top and bottom thicknesses and taper angle.

close: K_x had an error of 13%, K_y had an error of 27%, K_z had an error of 31%, K_{θ_x} had an error of 0.3%, K_{θ_y} had an error of 5% and K_{θ_z} had an error of 58%.

Errors in measurement could have also arisen from error in the capacitance probes. Some drift was observed during measurement and could have come from issues in grounding. The capacitance probes were also measuring from a surface, and there could have been surface irregularities, and such bumps could have added error to the readings. Sensitivity of the capacitance probes and a slight taper angle of the measurement stage could also have contributed to the errors, as well as thermal expansion of the structures during testing.

Table 4.1: A comparison of system stiffness values as determined by CF model, FEA model, measured fabricated model, and updated FEA model with taper angles.

Stiffnesses	Model Value	FEA Value	Measured Value	Updated FEA Value
K_x	0.644 N/mm	0.612 N/mm	0.740 N/mm	1.06 N/mm
K_y	0.644 N/mm	0.612 N/mm	0.877 N/mm	1.06 N/mm
K_z	3.43 N/mm	3.6 N/mm	5.003 N/mm	7.023 N/mm
K_{θ_x}	27.7 Nm/rad	21.92 Nm/rad	27.59 Nm/rad	32.07 Nm/rad
K_{θ_y}	27.7 Nm/rad	21.92 Nm/rad	29.31 Nm/rad	32.07 Nm/rad
K_{θ_z}	2.09 Nm/rad	2.85 Nm/rad	5.05 Nm/rad	4.3 Nm/rad

4.2 Parasitic Motions

Parasitic motions are undesired motions in an unactuated direction. In this design, the parasitic motions were designed to cancel out, and are not seen in either the CF model or the FEA models. In the measurements taken of the fabricated flexure system there are a few detected parasitic motions. For some directions, the detected parasitic motion fall within the variability of the actuated directions, suggesting that it could be noise or error in the measurement technique. Table 4.2 compares the voltage readings from the capacitance probes measuring the parasitic error to the error (maximum value -minimum value) in the readings of the actuated directions.

Some of the larger parasitic motions are seen mainly the planar directions of x , y and θ_z . Since the flexure is so compliant, a small actuation in the direction could result in a detectable displacement. Undesired parasitic motions could have arisen from slight misalignment of the fishing line and the pulleys, which adds a perpendicular component of force. In the nanoink or final set up, linear voice coil motors would be used to directly actuate the stage rather than the weights and pulleys, eliminating this issue. The actuators could also be used to compensate for the parasitic motions.

Table 4.2: Voltage readings from capacitance probes measuring displacements in the parasitic directions compared to the variation (max – min) of the actuated directions. Due to availability of capacitance probes, only five directions could be measured at once.

	Error in actuated directions (V)	Error ΔX (V)	Error ΔY (V)	Error ΔZ (V)	Error θ_x (V)	Error θ_y (V)	Error θ_z (V)
ΔX	2.29	–	0.713	0.103	0.08	N/A	0.98
ΔY	0.46	1.01	–	0.001	0.001	N/A	0.381
ΔZ	0.14	0.09	0.11	–	0.11	N/A	0.23
θ_x	0.30	0.69	0.49	0.215	–	N/A	0.36
θ_y	0.19	0.27	0.80	0.19	N/A	–	0.83
θ_z	1.38	1.69	0.41	0.20	0.16	N/A	–

Chapter 5

Conclusions and Future Work

The design of an x-y- θ_z stage using CFs seeks to demonstrate the functionality of CF design rules by applying them to a case study. By utilizing the CF rules for the design process and optimization, x-y- θ_z stage design brought forth the advantages and disadvantages of using cylindrical flexures for an x-y- θ_z stage in general, and demonstrated the usability of CF rules. This study sets an example for using CF design guidelines, making more flexure design tools available, expanding the design space, and helping others design with CFs for other functional requirements.

Through this study, it was found to be possible to meet the functional requirements and design goal for a CF flexure system that better positions the AFM tip for dip pen nanolithography. The design process revealed the benefits and challenges of using cylindrical flexures to design an x-y- θ_z stage by using the CF rules to model the system. The CF model predicted the final measurements quite closely, despite variability in the measurements and simplifications in the model. The stiffness of the system in the θ_z direction, K_{θ_x} , when comparing the model to the measured values, had an error as small as 0.3%, but in K_{θ_z} , the error was around 58%. This could stem from more complicated tip boundary condition effects not taken into account by the model, or error in measurement of the fabricated flexure. The CF design rules greatly informed the design, reducing time spent on FEA by quickly narrowing in on successful designs.

The final monolithic design allows for easy fabrication and requires no assembly. CF flexures also provide much larger ranges before yield and create a much thinner system, providing a solution if depth is constrained. However, due to the nature of CF elements, the stiffness ratios limited the constraints, suggesting that r -compliant CFs may be better suited for a six degree of freedom flexure system. In iterating through the many design options, there may be space for a 6 degree of freedom flexure in enhancing the simple four-element flexure with 180 degree sweep angle. Although there are possibilities for 6 DOF stages, CF x - y - θ_z stages are indeed viable and could be used to fill needs that straight-beam flexures cannot. Future work to address for a CF x - y - θ_z stage could include furthering system configuration designs to further better the stiffness ratios.

The CF element and system models corroborated by FEA helped determine the correct angles, radii and sweep angles much faster than using FEA alone. This research implements CF design guidelines and develops more specific guidelines regarding design of a CF x - y - θ_z stage. Beyond x - y - θ_z stages, this work lays the groundwork for using cylindrical flexure element rules to design radial-compliance CF systems in general. In designing for the DPN specific case study and applying the CF rules to creating a flexure, the guidelines and knowledge of CF flexure designs have increased for future use. Developing design guidelines for CF systems is a key step to furthering the field of cylindrical flexures, helping CFs address current design challenges and become more in precision engineering applications.

Bibliography

- [1] M. J. Telleria, M. L. Culpepper, and D. Weitz, "System Level Optimization of a Cylindrical Flexure for Linear Motion Guidance," *Proceedings of the 2010 ASPE Annual Meeting*, 2012.
- [2] S. Awtar, "Synthesis and Analysis of Parallel Kinematic XY Flexure Mechanisms," Massachusetts Institute of Technology, PhD Thesis, 2003.
- [3] J. B. Hopkins, M. L. Culpepper, "Synthesis of precision serial flexure systems using freedom and constraint topologies (FACT)," *Precision Engineering*, Vol. 35, pp. 638-649, 2011.
- [4] M. J. Telleria and M. L. Culpepper, "Understanding the drivers for the development of design rules for the synthesis of cylindrical flexures," *Mechanical Sciences*, vol. 3, no. 1, pp. 25-32, Apr. 2012.
- [5] M. J. Telleria, "Design Rules and Models for the Synthesis and Optimization of Cylindrical Flexures," Massachusetts Institute of Technology, PhD Thesis, 2013.
- [6] M. L. Culpepper. Massachusetts Institute of Technology, 2.72 Elements of Mechanical Design, Lecture 9 Slides, "Flexures" [PDF document] Accessed April 2013, http://pcsl.mit.edu/2_72/lectures/2013-Lecture_09_Flexures_v1.pdf.
- [7] M. A. C. Thomas, "Design, Fabrication and Implementation of a Flexure-based Micropositioner for Dip Pen Nanolithography," Massachusetts Institute of Technology, M.S. Thesis, 2012.
- [8] J.W. Ryu. D.G. Gweon, K.S. Moon, "Optimal design of a flexure hinge based XY θ wafer stage," *Precision Engineering*, Vol. 21, No.1, pp. 18-28, June 1997.
- [9] L.C. Hale, "Principles and Techniques for Designing Precision Machines," Massachusetts Institute of Technology, PhD Thesis, 1999.
- [10] R. D. Piner, J. Zhu, F. Xu, S. Hong, C. A. Mirkin, " 'Dip-Pen' Nanolithography," *Science*, Vol. 283 No. 5402, pp. 661-663, January 1999.
- [11] Nanoink, "What is Dip Pen Nanolithography (DPN)," Accessed May 2012, <http://www.nanoink.net/technology.html>.

- [12] D. S. Ginger, H. Zhang, and C. A. Mirkin, "The Evolution of Dip-Pen Nanolithography" *Angew. Chem. Int. Ed.* Vol. 43, pp. 30-45. 2004.
- [13] H. Radousky, J. Camarero, A. Noy, "Working at the Nanoscale," Lawrence Livermore National Laboratories, Accessed April 2013, <https://www.llnl.gov/str/November02/Radousky.html>
- [14] Monticont "Linear Voice Coil Motors," Accessed April 2013, <http://www.moticont.com/voice-coil-motor.htm>.